DOTTORATO DI RICERCA IN INGEGNERIA INFORMATICA

DIPARTIMENTO DI INGEGNERIA CHIMICA, GESTIONALE,

INFORMATICA, MECCANICA

ING-INF/05

SMART TECHNIQUES FOR FAST MEDICAL IMAGE ANALYSIS AND PROCESSING

IL DOTTORE
Ing. Luca Agnello

IL COORDINATORE
Prof. Salvatore Gaglio

IL TUTOR
Ing. Salvatore Vitabile

CICLO XXV

ANNO CONSEGUIMENTO TITOLO - 2015

Abstract

Medical Imaging has become an important transversal applications and research field that embraces a great variety of sciences. Imaging is the central science of measurement in diagnosis and treating diseases. The effort of the technological progress has made possible human imaging starting from a single molecule to the whole body.

The open challenge is to treat the huge amount of medical informations with the use of smart and fast techniques that allows clinical and images data analysis and processing.

In this ph.D. Thesis, many issues have been addressed and a certain amount of improvement in various fields have been produced, such as biometry, organs and tissues segmentation, MRI thermometry, medical reports retrieval and classification.

The topic prefixed at the beginning of this ph.D. route was to analyze, understand, and give a step over to various kind of problematics related to Medical Images and Data analysis, working closely to radiologist physicians, with specific equipments, and following the common denominator of fast and smart methodologies applied to the medical imaging issue.

A series of contribution have been carried out in fields such as:

- proposing two different kind of multimodal biometric authentication systems that investigates fingerprint and iris fusion and processing;
- applying expert systems to the issue of data validation, comparing and validating data to two different methodologies that assess liver iron overload in thalassemic patients;

- addressing and improving non-invasive referenceless thermometry by using Radial Basis Function as interpolator;
- applying the multi-seed region growing method to the segmentation of CT liver dataset;
- proposing a novel unsupervised voxel-based morphology method for MRI brain segmentation by using k-means clustering and neural network classification;
- proposing a novel ontology-based algorithm for information retrieval from mammographic text reports.

The above work has been developed with the cooperation of the medical staff of the “Dipartimento di Biopatologia e Biotecnologie Mediche e Forensi” and the “Scuola di Specializzazione in Radiodiagnostica" of the Università degli Studi di Palermo.

All the proposed contributions show good performance using the standard metrics. Most of them have produced scientific publications in computer science venues as well as in radiological venues. In addition, some specific frameworks, such as OsiriX, have been used to improve usability and easiness of the developed systems.

Contents

Chapter 1

Introduction

The medical imaging field is becoming nowadays increasingly important to human body imaging, for diagnostic and for treatment purposes. It incorporates several medical imaging techniques and got the important goal of the health's improvement all over the world.

1.1 Smart and Fast Medical Imaging

Medical imaging is a complex field and encloses several experts and expertise in different fields, such as physicians, engineers, biologist, physics and so on, and several equipment for diagnosis of diseases' course and treatment purposes, such as Magnetic Resonance Imaging (MRI), Computerized Tomography (CT), Positron Emission Tomography (PET), and many others specific equipment.

The role of medical imaging is totally transversal to the disciplines of medicine, computer science, electrical and electronics engineering, mathematics and data computation. It is necessary to develops algorithms in order to solve complex problems annexed to image visualization, clinical data retrieval, statistics and many other addressed issues related to the world of discovery and care about human' health.

The main focus is related to knowledge and clinical information extraction from different kinds of heterogeneous data: for the computation analysis of the images and data, it is necessary to develop smart and fast algorithms that can address all the issues related to the medicine field. This methods can be regrouped into several categories, that spreads in image segmentation, data classification and clustering, data reconstruction, brain morphometry, expert systems, biometric recognition, MRI thermometry, with the wide use of:

- Smart techniques: intelligent algorithms that rely on artificial neural networks, data clustering, and interpolation of data and functions;
- Fast methodologies: fast means an ad-hoc development of software that enable medical people to do job/research in a faster way (e.g. segmentation of hundreds of images all at once), and ad-hoc implementation of algorithms in dedicated hardware.

Medical data are not only related to medical images, but also includes medical reports written as free and unstructured text. Nowadays, the trend is to push most of the efforts also on information retrieval from medical reports and laboratory analysis. This data mining and information extraction, and conversion of unstructured data in structure data, is possible with the help of Big Data methodologies and soft-computing algorithms (i.e. ontologies and semantic and syntactic similarity).

It is necessary, however, understand that the medical imaging and medical data analysis and processing shouldn't be only for a strict group of expert physicians and researchers, but it should be available to all the people in-

volved in the medical imaging issues.

The technology and the computational power are nowadays enough mature and widespread: a big effort is necessary now to address all the power of calculators to analyze and process a huge quantity of data in the best and fastest possible way, and to mix all the heterogeneous data in order to obtain an information with a big data quantity and quality.

Smart algorithms and fast elaboration are the keywords for the care of each of us. Easiness and diffusion of ad-hoc algorithms and software appositely developed can have an huge impact on effectiveness of the work of all specialists involved in diagnosis and treatment of diseases.

In this ph.D. Thesis, specific aspects of medical imaging analysis and processing has been investigated and a contribution in several fields has been carried.

1.2 Bioimaging

With the "bioimaging" term we refer to structural and functional images of living things. Indeed, medical imaging can be considered a sub-branch of biomaging. The bioimaging science comprises the techniques designed to create images of the human body, both for clinical purposes (such as diagnosis and disease' follow-up), or to study the biometric traits of the humans.

1.2.1 Medical Images

The great multitude of heterogeneous data characterizes the field of medicine and medical imaging. With the terms of medical imaging we refer to the

process that allows to observe an internal area of the body in a non-invasive way. Radiology is the branch that mainly is involved for this purposes.

Many imaging techniques are available, such as CT, MRI, fMRI, Mammography, PET and many others. All the scans are almost always stored in a particular data format, called DICOM protocol.

MRI is a multi-parameter and multi-planar technique, which allows to capture images of axial, sagittal, or coronal planes without moving the patient, in order to obtain images of the internal structure of the body, to highlight pathological or physiological living tissues.

The images that can be acquired by MRI are mostly of two types:

- T1-weighted images: the time T1, or longitudinal relaxation time is a measure of the time for which the protons to return to the initial equilibrium conditions, through the transfer of energy to the surrounding microenvironment (lattice), in order to obtain a T1-weighted SE sequence, using a short TR (relaxation time) associated with a short TE (echo time). On average, the living tissue immersed in a magnetic field intensity of 0.1-0.5 T have a T1 comprised between 300 and 700 milliseconds. On T1-weighted images, the cerebrospinal fluid (CSF) is dark while the fat is brilliant. The structures of the CNS (white and gray matter) have intermediate signal intensity.

- T2-weighted images: the T2, or transverse relaxation time, is a measure of the time taken by the spin of protons to get out of sync. This progressive desynchronization will void the transverse magnetization. A sequence to get a T2-weighted sequence will have a long TR associ-

ated with a long TE. The water has, therefore, a long T2. In biological tissues, T2 is between 50 and 150 milliseconds. Liquids or at least very hydrated tissues, appear bright white in T2-weighted images.

Figure 1: An example of MRI T1-w and T2-w acquisition of a brain.

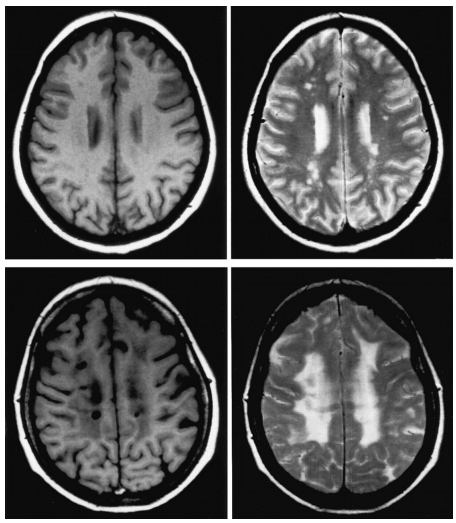

CT is a diagnostic imaging technique, which uses ionizing radiation (X-rays) and allows to reproduce sections or layers (CT) of the body patient and three-dimensional processing. For the production of images is required the intervention of a data processor (computer).

Figure 2: A CT acquisition of the liver.

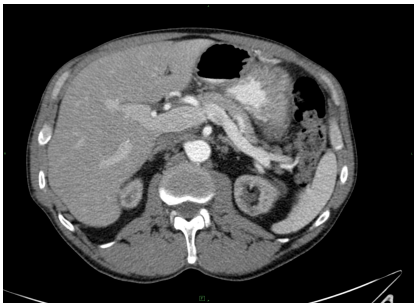

The law of absorption of X-rays explains how, given a beam of X-rays of a certain initial intensity exponentially decreasing in extent to the mass attenuation coefficient and the path made in the medium.

Then the X-ray beam through an object will be attenuated by materials with an high atomic number, the more energy will be low and the greater will be the thickness crossed; vice versa, if it crosses a low density material, the attenuation will be less. This is why on radiographs analog objects appear clear to higher density (maximum attenuation) and the lower-density objects appear darker (minimum attenuation).

The principle on which the tomographic reconstruction is based is the involving of many radiographic acquisition of the same object at different angles, and in this way is it possible to reconstruct the object in its third dimension. To obtain the third dimension, complex mathematical algorithms such as filtered backprojection methods (Filtered Back Projection algorithm, FBP) if the X-ray beam is parallel are used, the Feldkamp method if the beam is conical, or iterative methods are used. After applying reconstruction algorithms, is obtained a digital image that represents the distribution of the density of the object in one of its internal section (slice) and whose smallest element is called voxel, as it is a volume element. The smaller the volume represented by a voxel is, the greater the spatial resolution we obtain.

1.2.2 Biometric Templates

Fingerprints are characterized by a series of ridges; between two adjacent ridges there is a valley. Careful analysis of images acquisition can find other peculiarities, distinguished in macro and micro-features.

Macro-features fingerprint are generally used for images classification, and they can be divided into:

- Singularities: are regions where the ridges have a particular trend (pronounced curvatures, reclosing, confluence, etc...) and they belong to three distinct classes: loop, delta junction and whorl. In these areas the "drawing" of the crests is in the shape of O, Δ, U;
- Flow lines: hypothetical lines ideally parallel to a group of contiguous ridges; since not being real lines, the flow lines are not precisely defined;
- Directional image: is a matrix of the directions obtained by overlapping a grid with a series of nodes and thinking of drawing in each node a vector with a parallel direction to the flow line passing through the node itself;
- Ridge count: is a parameter that indicates how the ridges are close in a certain region and is represented by the number of ridges intersecting a segment having as its extreme two hypothetical points on the fingerprint.

On the contrary, in a fingerprint there are local discontinuities along the ridges: terminal points and bifurcation points called minutiae. The type of discontinuity in the lines determines the type of minutia. Each minutia is uniquely identified by:

- Type: terminal point and bifurcation point;
- Location: it is represented by minutiae coordinates in the Cartesian system representation;

- Orientation: it represents the angle formed by the vector which determines the direction, and the direction of the minutia with the horizontal axis.

Figure 3: a) Original fingerprint; b) image enhanced by Gabor and Segmentation algorithms; c) fingerprint after thinning algorithm.

a) b) c)

The iris is an increasingly used biometric template. The visible part of the iris is divided into two main zones which are often different for the color: the ciliary zone and the area separated from the pupillary internal collars (hedge) that has a zigzag pattern structure, called Collarette.

Iris features are random and they aren't dependent by genetic factors (the pigmentation color is the only genetic feature). Moreover, in each person iris differs from one eye to another. It exhibits about 266 features against 90 of the fingerprint; the iris temporal invariance is guaranteed by cornea and it isn't subject to diseases that can change its appearance. The probability to find two identical irises is one in 10^78, so the iris is a valid biometric identifier.

The biometric system phases are the following:

- Eye image acquisition: typically it is performed by a CCD camera, that tries to acquire with the maximum definition the human iris;
- Iris localization: iris is extracted from acquired image, localizing the portion of the image between external (limbo) border, and internal (pupil);
- Image normalization: the Cartesian coordinates system is modified into polar coor-dinates representation, because the iris area isn't constant but it varies in relationship to pupil expansion;
- Features extraction: micro (nucleus, collarette, valleys, radiants) and macro (frequency code extraction) features extraction;
- Coding: it consist in the pattern extracted construction of micro or macro features;
- Matching: it compares an acquired iris against an iris stored in a database, using a metric (i.e. Hamming distance).

Figure 4: Iris Collarette.

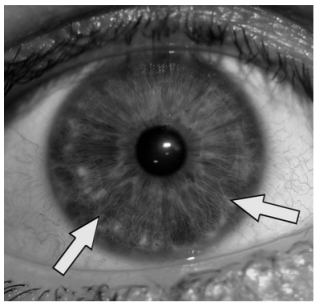

1.3 The OsiriX Framework

OsiriX is an open source software developed by Antoine Rosset which allows to realize image processing of medical images produced by special diagnostic equipment, such as MRI, CT, PET and so on. OsiriX is fully compliant with the DICOM standard.

The main purpose of OsiriX is the possibility to perform medical image processing in a multimodality and multidimensional way: in fact, it is possible to display images from 2 up to 5 dimensions and combine images obtained from different equipments, for example, a PET with a CT. In particular, the display includes 3D rendering techniques, such as volume rendering, surface rendering, MPR, MIP.

The software lets to interact with a PACS (Picture Archiving and Communication System), a system that allows to store images in DICOM format, to make queries regarding the information contained in these images and to make download pictures. To be precise, even the communication protocol with a PACS is specified by the DICOM standard.

OsiriX has been implemented in Objective-C, and is built at the top of COCOA, a platform designed to develop applications on MAC OS, and it is based on open source components that can be divided mainly into two levels: high level and low level libraries. OsiriX interacts only with the libraries of high level, through the API (Application Programming Interface) of the latter, which, in turn, communicate with the low-level libraries, responsible for interfacing with the hardware.

High-level libraries:

• VTK (Visualization ToolKit) : C ++ libraries and open source platform for graphics, image processing and 3D visualization;

• ITK (Insight ToolKit): C ++ libraries that implement open source and cross-platform segmentation algorithms and registration into two, three or more dimensions;

• Papyrus: platform library of C routines that facilitate the process of reading and writing DICOM images;

Low-level libraries:

• OpenGL: environment for development of 2D and 3D graphics applications. The standard provides the possibility of using the C, C ++, Fortran, Ada, Java;

• Quicktime: multimedia technology to develop video, sound, animation, graphics, text, interactivity and music;

• Xgrid: technology that allows to virtually bring together a group of MAC into a supercomputer, thereby capable of solving complex problems;

• GNUstep: object-oriented platform for the development of desktop applications in Objective-C based on the specifications of the application layer of the OpenStep NeXT (now Apple);

• COCOA [9]: object-oriented development environment designed to develop native applications MAC OS in Objective-C or Objective-C ++

1.4 DICOM Protocol

DICOM (Digital Imaging and Communications in Medicine) is the standard format used for the exchange of information between electronic devices and biomedical computing. The DICOM defines the standards for storing, view-

ing, printing and communication of biomedical information. Nowadays the DICOM format is widely used in hospitals and is establishing itself as the standard in both public and private health sector. The DICOM standard has been designed in order to achieve the following objectives:

- Obtain a standard for communication between acquiring medical images devices created by different manufacturers;
- Facilitate the introduction of new services that support the medical applications of the future;
- Where possible use existing international standards.

The DICOM standard describes:

- a set of protocols for network communications in order to establish how the devices respond to commands received;
- the syntax and semantics of commands that can be exchanged through these protocols;
- a range of services for storage on the file system;
- a file format for storing information biomedical;
- a directory structure that facilitates access to medical images and related information;
- the criteria for assigning to an implementation conformance to the standard, specifying which functions have the characteristic of interoperability to other compatible devices.

A DICOM file can contain a lot of information such as images, textual data, waveforms, etc.. In most cases a DICOM file does is encapsulate an image medical adding a variety of information from several sources. Among the most important:

- information about the image itself: resolution (height and width), color mode, the domain of colors, size of the voxel (volume element), etc.;
- patient information: name, age, weight, sex, etc.;
- information on the mode of acquisition: MRI, CT, ultrasound, etc.;
- information on the equipment used: manufacturer, model;
- medical information on the organization that carried out the acquisition;
- image storing in compressed or uncompressed (lossy or lossless) way.

DICOM files are generated by special medical equipment (scanners) in the case of Magnetic Resonance Imaging (MRI), and Computerized Tomography (CT).

1.5 Medical Data Ontologies

Most of the data in the medical field are not structured but on simple sheets of free text. An ontology describes the semantic similarity by means of similarity between concepts contained into unstructured text, aiding the information extraction of sensible data. Ontology-based methodologies that determine the semantic similarity between concepts in the documents to

compare are not limited to the lexical level but takes advantage of the relationships between concepts provided inside.

An ontology describes name, definition, properties and relationship between entities for a specific domain (i.e. medical domain). It usually use a glossary that defines all the terms and relationships among data. Common ontologies are composed of objects with determinate attributes and relationship, and rules (the logical inferences that can be drawn from an assertion). Axioms are statements asserted as a priori knowledge, and events are related in the changing of relations and attributes.

In the medical field, there is some example of medical ontology. For example, the Systematized Nomenclature of Medicine (SNOMED CT) contains diseases, findings, procedures, microorganisms and substances, their synonyms, and a wide range of relationships between concepts. Unified Medical Language System (UMLS) joins the concepts of different terminologies and ontologies used in biomedical systems and information services.

1.6 Thesis Outline

The remainder of the dissertation is organized as follows.

Chapter 2 describes the state-of-the-art that inspires the Smart and Fast Medical Imaging.

Chapter 3 presents an innovative approach that combines together fingerprint and iris templates for a Biometric Recognition System.

Chapter 4 presents a medical application that uses an Expert Systems that validates a novel method with a state-of-the-art method employing an artificial neural network (ANN).

Chapter 5 discuss about Radial Basis Function ANNs, used for interpolation (missing data reconstruction) purposes in MRI thermometry, validating the approach with two different kinds of subjects.

Chapter 6 describes two approaches for Image Segmentation, one using multiple-seed Region Growing approach for liver lesion, and the other one clustering and classifying voxels of MRI T1 brain datasets for VBM purposes.

Chapter 7 discuss the proposed Ontology-Based Retrieval System for Mammographic Reports, with test on a real mammographic dataset of 126 reports written in free text by expert radiologist.

In Chapter 8, all the experimental results are shown.

Finally, discussion and conclusion about this ph.D. path, and some possible direction for future research.

1.7 List of Publications

1. V. Conti, F. Sorbello, S. Vitabile, L. Agnello: *"Fingerprint And Iris Based Authentication In Intercooperative Emerging E-Infrastructures"*. Internet Of Things And Inter-Cooperative Computational Technologies For Collective Intelligence, Studies in Computational Intelligence, Vol. 460, 2013, pp 433-462, DOI 10.1007/978-3-642-34952-2_18, Springer.

2. L. Agnello, A. Farruggia, P. Toia, E. Murmura, M. Russo, E. Grassedonio, M. Midiri, S. Vitabile: *"A Novel Expert System for Non-Invasive Liver Iron Overload Estimation in Thalassemic Patients"*. The 8th International Conference on Complex, Intelligent, and Software Intensive Systems (CISIS-2014), Birmingham, UK, July 2-4, 2014. DOI

10.1109/CISIS.2014.16 3.

3. A. Farruggia, L. Agnello, P. Toia, E. Murmura, M. Russo, E. Grassedonio, M. Midiri, S. Vitabile: *"Liver Iron Overload MOnitoring in Thalassemia (LIOMOT) for classifying liver iron concentration in thalassemic patients trough an Artificial Neural Network (ANN)"*. Submitted to La Radiologia Medica, Springer.

4. A. Insalaco, L. Agnello, F. Midiri, L. Galbo, M.C. Galfano, M. Galia, et al.: *"Creazione di un Plug-In per il Software Open-source di Visualizzazione di Immagini DICOM OsiriX per lo Studio delle Variazioni Dimensionali e Densitometriche di Metastasi Epatiche in TCMS"*. Il Giornale Italiano di Radiologia Medica, 1 (Vol. 1), 625-629

5. D. Picone, L. Agnello, G. Lo Re, M. Galfano, A. Insalaco, F. Muscarneri, et al.: *"An Osirix Based Plug-in for the Study of Dimensional and Densitometric Changes of Hepatic Metastases on CT Images"*. In Proc. of ECR 2014. Wien : Springer-Verlag Germany, DOI 0.1594/ecr2014/C-0599

6. L. Agnello, C. Militello, C. Gagliardo, S. Vitabile: *"Referenceless Thermometry using Radial Basis Function Interpolation"*. Proc. of the International Conference on Computer Medical Applications (ICCMA 2014), World Symposium on Computer Applications & Research (WSCAR 2014), 1-6, DOI 10.1109/WSCAR.2014.6916834.

7. L. Agnello, C. Militello, C. Gagliardo, S. Vitabile: *"Radial Basis Function Interpolation for Referenceless Thermometry Enhancement"*. Proc.

of Italian Workshop on Neural Networks, Smart Innovation, Systems and Technologies, Springer. To be published.

8. L. Agnello, A. Comelli, G. Urso, S. Vitabile, E. Ardizzone: *"A Novel Technique for Voxel-Based Morphometry Analysis using K-Means and Neural Networks"*. Submitted to the International Journal of Imaging Systems and Technology, John Wiley & Sons Editors.

9. A. Comelli, L. Agnello, S. Vitabile: *"An Ontology-Based Retrieval System for Mammographic Reports"*, submitted to the IEEE Symposium on Computers and Communication, ISCC 2015 (6-9 July 2015), Larnaca, Cyprus.

Chapter 2

Review of the State-of-the-Art

In this section many aspects of Medical Imaging analysis and processing will be investigated, taking into account various issues and research fields related to computer science engineering, such as image segmentation, data analysis and clustering, function and data interpolation, neural networks, expert systems, and so on. A wide review of the state-of-the-art methodologies is necessary in order to understand the contribution produced by the present Thesis.

2.1 Fingerprint and Iris Biometric Recognition

E-infrastructures must support the development of heterogeneous applications for workstation network, for mobile and portable systems and devices. In this context and relating to all collaborative and pervasive computational technology a very important role is played by security and authentication systems, which represent the first step of the whole process [1].

Figure 5: a) Terminal point; b) Bifurcation point; c, d) Boundary minutiae removal.

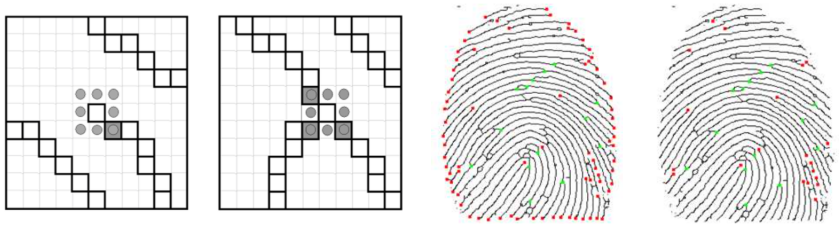

Biometric authentication systems represent a valid alternative to conventional authentication systems providing robust procedures for user authentication.

The first step for fingerprint recognition is a pre-processing phase, that consists of:

- Normalization: it allows standardizing pixel intensity, so they can have value in a fixed range;
- Gabor filtering: a Gabor function is realized by modulating a sine wave or a co-sinusoid with a Gaussian function in order to obtain spatial and frequential information. In fact, the image decomposition is carried out through a pair of quadrature Gabor filters, the 2D Gabor wavelet;
- Segmentation: it consists in separating foreground and background regions; foreground regions contain ridges and valleys of the fingerprint. Generally, the background regions are characterized by a very low level of variance in contrast to foreground that has high variance, for this reason the variance threshold method is used ;
- Thinning: in order to reduce the ridge thickness to a single pixel (1 pixel-wide), the Zhang-Suen thinning algorithm can be used; the image is binarized and the algorithm is iteratively applied until no pixel is candidate for elimination. This step is necessary to minutiae localization.

After the pre-processing phase,we can proceed to matching phase.

Matching is the process that establishes the similarity degree between two fingerprints using the above descripted features. The main difficulties in the matching phase are due to changes of factors such as translation, rotation and the epidermis that can be different during each acquisition. The most common methods for fingerprints matching proposed in the literature are:

- Matching based on the correlation: it consists in "overlapping" two images in order to calculate the difference of the corresponding pixels. This type of comparison requires a phase of fingerprint images alignment (image registration);

- Matching based on minutiae: it is the most common used technique. Minutiae are extracted from the fingerprint image and stored as a set of points. The comparison consists in finding the maximum coincidence between same types of minutiae in corresponding positions between the online acquired and stored fingerprint.

Algorithms used for macro-features extraction are based on the patterns analysis of singularities regions and topological information such as relations between different regions [3]. Macro-features are generally used to classify fingerprints in five macro- categories [4].

Iris features are random and they aren't dependent by genetic factors (the pigmentation color is the only genetic feature). Moreover, in each person iris differs from one eye to another. It exhibits about 266 features against 90 of the fingerprint; the iris temporal invariance is guaranteed by cornea and it isn't subject to diseases that can change its appearance. The probability to find two identical irises is one in 10^78, so the iris is a valid biometric

identifier.

The Gabor filter is widely used in frequency-domain based approaches to obtain and codify localized information. The Log-Gabor filter implementation, proposed by Field [5] can be used. Log-Gabor filter can be constructed with arbitrary band. It's a Gabor filter constructed as a Gaussian on logarithmic scale. The filter frequency response is:

$$G(f) = exp(\frac{-(log(\frac{f}{f_0}))^2}{2(log(\frac{\sigma}{f_0}))^2} \tag{1}$$

where f_0 is the center frequency and σ determines the bandwidth of the filter. In the second method implemented in [6], the iris has been encoded using the Log-Gabor filter. In particular has been used the algorithm written by Libor Masek, which consists in considering each row of the normalized image, as a 1D signal that is convolute with the 1D Log-Gabor filter. The output filter is then quantized into four levels. The coding process is illustrated in [7]. The encode function generates a biometric template of normalized iris and a mask that represents noise in the image: this information will be stored in a database and it will represent a user.

Multimodal systems can be classified in according to the number of sources and bio- metric number of "samples" used [8]. The main feature of a multimodal system is to combine different information to arrive at a decision. We can distinguish different types of fusion and consequently different systems architectures [9], [10]. In relation to the decision policy founding fusion algorithms, there are two possible approaches: the *pre_mapping* fusion strategy applied before the matching phase and the *post_mapping* fusion

strategy applied after the matching phase.

Pre_mapping fusion has two subcategories: sensory data level fusion, in which data coming from sensors are combined before the remaining processing steps; and a features extraction fusion level, in which the extracted biometric information coming from different modalities are fused before the remaining processing steps.

In *post_mapping* fusion, there are two subcategories, as well: a matching score level fusion (also known as level review), in which the results of two independent matching systems are combined with a weighted rule; and the decision level fusion, in which a decision system is used to process unimodal system output decision. Widely-used *pre_mapping* fusion approaches refer feature set fusion, while widely-used *post_mapping* fusion approaches refer independent matching score fusion.

2.2 Data Clustering and Data Mapping

Clustering term indicates the task of grouping a multitude of objects into groups (or clusters). The object will be grouped in the same group if some similarity measure is satisfied, i.e. the object are more similar to each other than those present in other clusters. A specific pattern inside a cluster contains a similar pattern than a pattern belonging to another cluster.

Clustering is a difficult problem, main task of data mining, and a widely used technique in many fields such as image analysis, information retrieval and pattern recognition.

Figure 6: Data Clustering.

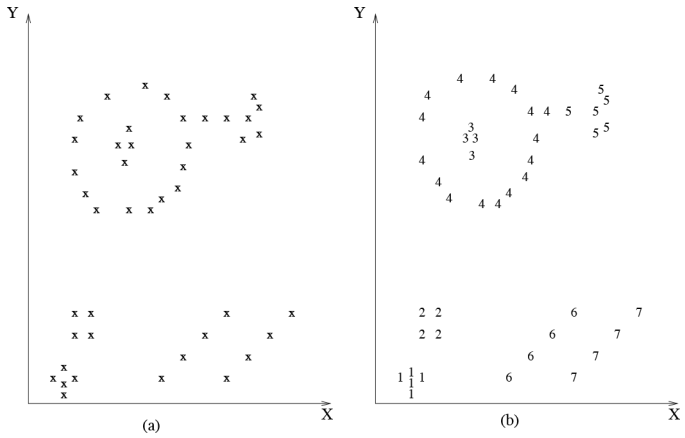

As depicted in Figure 6, points that belongs to the same group have the same label. The great multitude of existing techniques for similarity measurement between data, labeling of the data, and clustering, allowed a wide development of clustering techniques. Luckily, in pattern analysis, data mining, image segmentation, there is always some kind of information that make possible to the decision algorithm to make some hypothesis about data grouping. In this way clustering becomes appropriate for assess relationships among the data points and do the clustering process.

2.2.1 K-Means Clustering

Partitional clustering divides a given set of objects in a set of clusters, disjoint among them. A dataset composed of N points is clustered into k clusters, with $N \geq k$. Each k partition represents a cluster, that contains:

- at least one point, and
- each point belongs to exactly one cluster.

$K - means$ clustering is the simplest and most common used partitional algorithm, and it tries to minimize an objective function, for the instance:

$$\sum_{i=1}^{k} \sum_{j=1}^{|C_i|} Dist(x_j, center(i)) \tag{2}$$

where $|C_i|$ is the number of objects in the i cluster, and $Dist(x_j, center(i))$ is the distance between the point x_i and the $i - th$ centroid.

The partitional algorithm results in clustering the data space into Voronoi cells. The algorithm starts choosing the number of desired cluster, and with i random initial partition centroid, reassigning the objects to clusters until the objective function reaches the convergence (aftern a certain numbers of iterations).

The $k - means$ clustering is different, for example, from fuzzy partitioning, where a given point can belong to many clusters. It is widely used because his implementation facility, but on the other hand the algorithm is sensible to the initial random choice of centroid, that can lead minimization function to stop in a local minima.

Figure 7: K-Means partitional clustering. The objects have been divided in k=3 clusters.

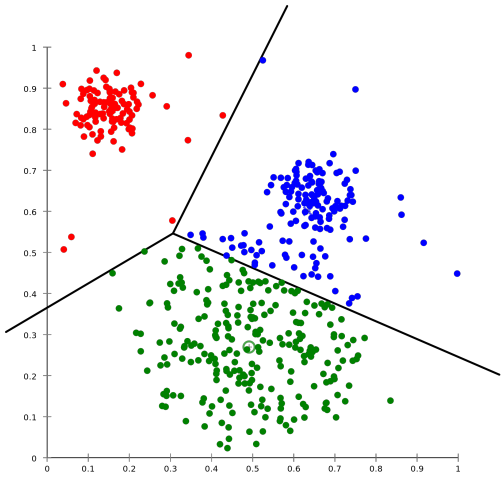

The workflow of the algorithm is as follows:

1. choose randomly k cluster centroids that coincides with k random patterns;
2. assign each pattern to the closest center;
3. recompute the centroids using the cluster membership;
4. and if the minimization function does not converge, repeat the steps from 2 to 4.

2.2.2 Neural Networks

An Artificial Neural Network is a mathematical model that is created from imitating the human though process, simulating the (human) biological neu-

rons. The ANN is widely used in data mining, image processing, and for approximate functions with a certain number of input, elaborating informations with the capability of learning, generalization and adaptation.

A Neural Network is composed of artificial neurons that send signals each other. The network can approximate a function with multiple inputs and outputs, and it is widely used for tasks like classification, clustering, function approximation.

There are various kind of neural network, like self organizing map or recurrent neural network, but the most common kind of ANN is the feed-forward. In this context we will consider this kind of network, and the back-propagation learning algorithm used to train the ANN.

In the feed-forward NN, the information goes in one only direction, starting from input, passing through the hidden layer and going to the output of the network, without any cycle or loop.

Figure 8: The structure of the A.N.N.

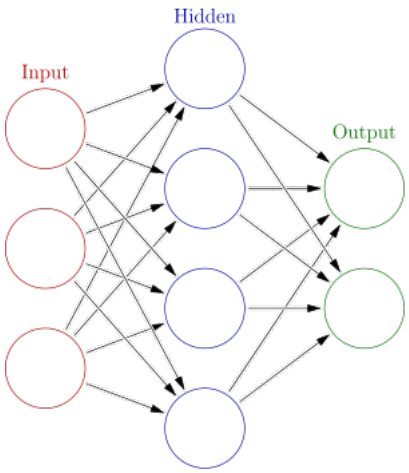

Each input and output is weighted by using weights w_{ij} and shifted by a specific bias factor. The goal of the network is to, given a function, learn the weights and the bias factor that will shift the output result. A neuron got an input that connects a neuron to another or directly to the input of the network, and an output. Each neuron has an activation function associated with it. The output of a single neuron is computed by weighting sum of inputs, adding bias and feeding the sum as input to the activation function of the neuron. So the output of the activation function is the output of the neuron, according to the following Equation:

$$Output = A(\sum_{k} w_k I_k + bias) \tag{3}$$

where A is the activation function of the neuron, w_k is the weight of the $k-th$ in-edge, I_k is the input carried across the $k-th$ in-edge, and $bias$ is the bias of the neuron. In the learning phase, the neural network will learn weights and biases until a condition is satisfied, i.e. the error between the training data and the output is minimum. Easily, it is possible to train data by using couples of inputs and outputs (X_i, Y_i). X_i denotes the input to all input neurons, while Y_i is the desired output. The training dataset is computed as $D = Union((X_i, Y_i))$. The sum of squares error, in accord to training data D is computed as:

$$SSE(D) = sum((Y_i - Z_i)^2) \tag{4}$$

where Z_i is the set of desired network's output, given a certain input X_i.

In the back-propagation learning the algorithm trains the neural net-

work and updates weights and biases in each step, minimizing a gradient minimum of the error respect weights and biases. The algorithm for learning an instance can be divided into three phases:

1. given the input set X_i, calculate Z_i, the output of the network;
2. calculate Blame: if Y_i is the desired value for Z_i, and if they are different, there is some error that is computed as a blame for each neuron. Blames are used to adjust weights and biases;
3. adjust weights and biases, performing the gradient descent.

After the training session, the learning is complete and the neural network can be used for its purposes.

2.2.3 Expert Systems

Expert Systems (ES) emulate the ability of humans in decision-making processes [11], implementing inference procedures in complex problem solving [2], [3]. They are able to lead its expertise in a specific knowledge domain [4]. Computational Intelligence methodologies are characterized by adaptivity, errors-tolerant, inspired by biological or cognitive principles, parallel in nature, and operating in the numeric domain [5]. Nowadays people are beginning to use Expert Systems for supporting their everyday life. The logic implemented in ES can be based on Computational Intelligence derived methods, such as the Artificial Neural Network, Support Vector Machine, Bayesian Network, Fuzzy Logic.

One of the goals of Expert Systems is the implementation of inference procedures for complex problems solving. ES can be used for analyzing and

understanding future direction of interesting application fields, such as environmental sciences, agricultural sciences, transportation systems, economic sciences, life sciences.

ES can be also used for data mapping and correlation between one or more classes of heterogeneous data.

The authors of [13] discuss the design and evaluation of an intelligent sorting system for open and closed-shell pistachio nuts. The system includes a feeder, an acoustical part, an electronic control unit, a pneumatic air-rejection mechanism and a ANN classifier. A prototype system was set up to detect closed-shell pistachio nuts by dropping them onto a steel plate and recording the acoustic signal that was generated when a kernel hit the plate. The recognition is based on combined PCA of impact acoustics and ANN classifier. Authors evaluated proposed system computing the mean square error (MSE), correct classification rate (CCR) and coefficient of correlation (r). Experimental results establish the superior performance of the proposed approach when compared to prior techniques reported in the literature or used in the field.

In [14], the authors report the development of an expert system for fruit tree disease and insect pest diagnosis based on artificial neural network and geographic information system (GIS). A multiple knowledge acquisition approach was adopted for creating the knowledge of the system, using neural networks to predict the development tendency of fruit tree disease and insect pest. The system was trained with 11 years meteorological information and occurrence status of fruit tree disease and insect pests in orchards of Yantai city. The ring spot, a fruit tree disease, was chosen as the research object to

compare the predicted value with the actual value in this study.

In [15] and [50], the authors exploit the Radial Basis Function (RBF) network to provide a method for temperature change measurements during thermotherapy. The effectiveness of the proposed approach has been demonstrated with Magnetic Resonance guided Focused UltraSound (MRg-FUS) sonications on ex-vivo animal muscle, and on a real dataset of female patient undergone to uterine fibroid surgery. A significant improvement of the referenceless thermometry method, against classical PRF thermometry and polynomial referenceless thermometry, has been demonstrated.

In [16], the authors present an Expert System for medical diagnosis of the most common skin disease, the scabies, using Artificial Neural Network (ANN) based classifier. The system helps the medical professional in making effective treatment to patient, by reducing unnecessary costs. The data used in the implementation and testing of the ANN were collected from the leading Skin clinics of Vadodara, India. The system achieves 95% success.

In [17], the authors describe a project work aiming to develop an Expert System for diagnosing heart disease using neural network technique. The Support Vector Machine (SVM) and RBF have been applied over the data for the experiment. The authors focus on the research and development of a web-based clinical tool designed to improve the quality of the exchange of health information between health care professionals and patients. This system is experimented on various medical scenarios and exhibits satisfactory results.

In [18], the authors propose an Expert System based on ANNs and SVMs to aid the specialist in the diagnosis of Parkinson disease. The authors

exploit these two classifiers because they produce a good performance in the diagnosis task. This ES is used for reinforce and complement the diagnosis of the specialists and their methods in the diagnosis tasks. Data recorded during 195 examinations carried out on 31 patients was used to verify the capacity of the proposed system. The results show an high accuracy of around 90%.

2.3 Thermometry in Magnetic Resonance Imaging

Minimally invasive thermal therapy of oncological lesions benefits from near real-time Magnetic Resonance Imaging (MRI) guidance. MRgFUS (Magnetic Resonance guided Focused UltraSound) is a new and non-invasive technique to treat different diseases in the oncology field, which uses Focused Ultrasound (FUS) to induce necrosis in the lesion. This is due to the attractive properties of MRI, such as its non-invasiveness, lack of ionizing radiation, and the good spatial and temporal resolution in any scan orientation. However, it is the ability of MRI to construct maps of in-vivo body temperature that make it particularly well suited for guiding and monitoring thermal therapy.

Thermal therapy can be divided into two regimes. The first one is low-temperature hyperthermia, where temperatures in the range of 43÷45°C are applied for a time of several tens of minutes to kill cancer cells or to sensitize them to cytotoxic agents and/or radiation [19]. The second one is high-temperature thermal ablation, where temperatures in the range of 50÷80°C (or higher) are applied for a shorter amount of time to rapidly coagulate the tissue and induce necrosis through processes such as protein denatu-

ration. Non-invasive temperature monitoring is feasible with MRI, based on the temperature sensitivity to the MR parameters such as the Proton Resonance Frequency (PRF), the diffusion coefficient, T1 and T2 relaxation times, magnetization transfer, the proton density, as well as temperature sensitive contrast agents.

2.3.1 Proton Resonance Frequency (PRF) Shift Thermometry Temperature change measurements during ultrasound thermo-therapies can be performed through magnetic resonance monitoring by using PRF shift thermometry. It measures the phase variation resulting from the temperature-dependent changes in resonance frequency by subtracting one phase baseline image from actual phase. A good overview of MRI temperature methods is shown in [20]. Proton spectroscopic imaging, like PRF shift thermometry uses phase mapping and the temperature-induced water proton chemical shift. Here the frequency shift is calculated from the MR spectra. MRI-derived temperature maps can be constructed using a Gradient-Recalled Echo (GRE) imaging sequence by measuring the phase change resulting from the temperature-dependent change in resonance frequency. In order to eliminate temperature-independent contributions (e.g. due to B_0 field inhomogeneities), one or more baseline images are usually acquired before thermal therapy and subtracted from images during heating. The phase difference images are proportional (i) to the temperature-dependent PRF change and (ii) to the echo time TE, and can be converted to a temperature

change ΔT by the following Equation:

$$\triangle T = \frac{\varphi(T) - \varphi(T_0)}{\gamma \alpha B_0 T E} \tag{5}$$

where $\varphi(T)$ is the phase in the current image, $\varphi(T_0)$ is the phase of a reference (baseline) image at a known temperature, γ is the gyromagnetic ratio, $\alpha = -0.01 ppm/^{\circ}C$ is the PRF change coefficient, B_0 is the magnetic field strength, and TE is the echo time.

2.3.2 Referenceless Thermometry

MRgFUS thermal ablation represents an innovative approach used to treat a wide range of diseases [21][22]. Motion of anatomical region undergone to the MRgFUS treatment is one of the most prevalent problem for temperature monitoring with PRF phase mapping. For temperature evaluation during thermal treatment, motion artifacts can be divided into two categories: intra-scan motion and inter-scan motion, based on the time scale of the motion with respect to the image acquisition time.

Intra-scan motion is caused by movement of an object during MR image acquisition, resulting in a poor quality image with typical blurring and ghosting artifacts. These motion artifacts are not specific to PRF temperature imaging and can be reduced by accelerating the image acquisition.

Inter-scan motion is due to motion or displacement of an object between the acquisitions of consecutive images. Methods for temperature estimation in presence of motion can be divided into two categories: (i) methods based on a multi-baseline strategy and (ii) methods based on a referenceless

strategy.

Multi-baseline methods collect background phase information at various stages of the respiratory and/or cardiac cycle prior to heating, so that baseline data exist for all positions of the organ. The baseline subtraction is then performed by matching the image acquired during heating with the corresponding stored baseline data in order to mitigate motion-induced misregistration. The selection of the corresponding baseline image is performed by determining the organ's position with a navigator echo [23] or based on a similarity criterion, such as non similarity coefficients [24] or inter-correlation coefficients [25]. The multi-baseline methods require cyclic organ motion in order to acquire a full set of all possible baseline images and require additional setup time to assemble the baseline library. They are generally much more robust to motion than conventional baseline subtraction, but remain sensitive to susceptibility changes during therapy.

Referenceless methods estimate heating from a treatment image itself, without a baseline image used as temperature reference. Operating under the assumption that the phase image surrounding the treated region has a soft and smoothed trend even under the heated area, referenceless or self-referenced thermometry methods fit a set of smooth, low-order polynomial functions to the surrounding phase [26] or to a complex magnitude image with the same phase using a weighted least-squares fit [27].

The extrapolation of the polynomial inside the heated region serves as background phase estimation, which is then subtracted from the actual phase to evaluate the phase difference before and after heating caused by ultrasound sonication.

2.4 Image Segmentation

The process of dividing the image into homogeneous regions, where all the pixels that correspond to an object are grouped together, is called segmentation. The regroupment of pixels into regions is based in relation to a homogeneity criterion which distinguishes them from each other. The criteria can, for example, be similarity values of attributes (color, texture, etc.), or spatial proximity values (Euclidean distance, etc.).

2.4.1 Spatial Image Segmentation

An image segmentation is typically defined as an exhaustive partitioning of an input image into regions, each of which is considered to be homogeneous with respect to some image property of interest (e.g., intensity, color, or texture).

The goal of segmentation is to simplify and/or change the representation of an image into something that is more meaningful and easier to analyze.

Figure 9: An example of segmentation. Here a MRI brain dataset is segmented in its three main tissues: Cerebro-Spinal Fluid, Grey Matter, White Matter.

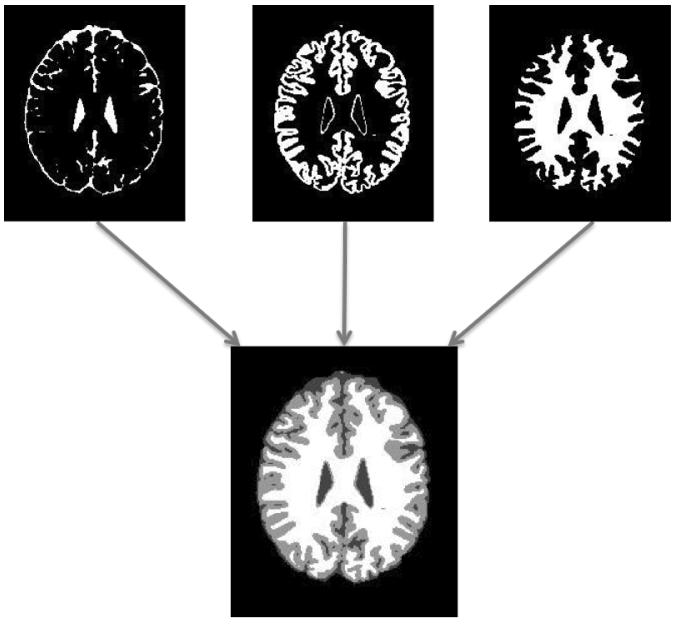

The final results of image segmentation can be expressed as follow: If I is the input image with N_r rows and N_c columns and measurement value x_{ij} at pixel (i, j), then the segmentation is $\varsigma = \{S_1, ..., S_k\}$ with the lth segment $Sl = \{(i_{l1}, j_{l1}), ..., (i_{lN1}, j_{lN1})\}$ consisting of a connected subset of the pixel coordinates.

Image segmentation is typically used to locate objects and boundaries (lines, curves, etc.) in images. More precisely, image segmentation is the process of assigning a label to every pixel in an image such that pixels with the same label share certain characteristics.

The result of image segmentation is a set of segments that collectively cover the entire image, or a set of contours extracted from the image edge detection). Each of the pixels in a region are similar with respect to some char-

acteristic or computed property, such as color, intensity, or texture. Adjacent regions are significantly different with respect to the same characteristic(s). When applied to a stack of images, typical in medical imaging, the resulting contours after image segmentation can be used to create 3D reconstructions with the help of interpolation algorithms like Marching cubes.

2.4.2 Region Growing Segmentation

Region growing has shown to be a very useful and efficient segmentation technique in image processing [28], [29]. Region growing in its simplest sense is the process of joining neighboring points into larger regions [30] based on some condition or selection of a threshold value. Seeded region growing starts with one or more seed points and then grows the region to form a larger region satisfying some homogeneity constraint. The homogeneity of a region can be dependent upon any characteristic of the region in the image: texture, color or average intensity.

One region-growing method is the seeded region growing method. This method takes a set of seeds as input along with the image. The seeds mark each of the objects to be segmented. The regions are iteratively grown by comparison of all unallocated neighboring pixels to the regions. The difference between a pixel's intensity value and the region's mean is used as a measure of similarity. The pixel with the smallest difference measured in this way is assigned to the respective region. This process continues until all pixels are assigned to a region. Because seeded region growing requires seeds as additional input, the segmentation results are dependent on the choice of seeds, and noise in the image can cause the seeds to be poorly placed.

2.4.3 Soft Computing Based Methods

In addition to traditional segmentation methods, there are soft-computing segmentation methods which can model some of human-like segmentation. Soft computing is a field that involves several methodologies, such as fuzzy logic and neural networks computing. The neural networks are widely used in several fields, and also in image segmentation.

Neural Network segmentation relies on processing images using an artificial neural network. After such processing, the decision-making mechanism labels the regrouped pixels of the image in accord to the category recognized by the neural network.

In [59], the authors exploits a method based on Self Organizing Maps (SOM) for clustering, with classification carried out by a self-organizing map (SOM), which is employed to obtain the main chromaticities present in the image. Then, each pixel is classified according to the identified classes. The number of classes is a priori unknown and the artificial neural network that implements the SOM is used to determine the main classes. The detection of the classes in the SOM is done by using a K-means segmentation.

The authors of [60] propose a neural network approach to medical image segmentation, based on SOM and a three-dimensional SOM architecture to create a 3D model, starting from 2D data of extracted contours.

A neural network learns in freedom from the data that are presented, without the obligation of having to comply to a model imposed a priori. Reviewing many times the training set, consisting of pairs of vectors that represent an input pattern and the desired output, the network change its

internal parameters (weights) in order to provide, in respect of each input, the required output.

2.5 Knowledge-Based Medical Reports Mining

Despite to the efforts of the national health care in the introduction of the electronic health record that allows to trace the patient's history, classification, improved search, reports extraction related to a particular information, control in data entry and support to the physician's decisions of the doctor, most of the data in the medical field are not structured but on simple sheets of free text.

Until now several approaches have been proposed to measure the similarity of documents with statistical techniques, data-mining and machine learning associated with the domain corpora. To fix these limitations, ontology-based methodologies that determine the semantic similarity between concepts in the documents to compare are used [61], [62], [63]. This semantic comparison is not limited to the lexical level but takes advantage of the relationships between concepts provided by ontology.

The knowledge-based approaches take advantage of the hierarchical structure of ontology and of domain knowledge modeled explicitly through concepts and semantic relations that allow various deductions from those known. These approaches typically determine the distance between two concepts of interest using techniques such as ontological depth, shortest path and the combination of these. The similarity is equal to the inverse of the ontological distance (Pedersen et al. [65] and Batet et al. [66]).

In the literature there are many research works on the comparison of

documents that use the semantic similarity.

Corley and Mihalcea [67] present a knowledge-based method to measure the semantic similarity of texts. While the great part of the work has focused on the search for the previous semantic similarity of concepts and words, in the application of these methods word-oriented similarity has not yet been explored. They introduce a method that combines a similarity word-to-word metric with a text-to-text metric, matching those words that are more similar to each other and by weighing their similarity with the corresponding score of specificity by demonstrating that this method exceeds traditional metrics of similarity on matching lexical word-oriented. The specificity of a word is determined using the inverse document frequency (IDF) in a large corpus.

Mihalcea et al. [64] has successfully used these algorithms to identify if two blocks are paraphrases each other. A similar system in the context of medical documents is the system XOntoRank [68], which provides the keyword research SNOMED on XML documents. Exploiting the ontological knowledge an open question is when dealing separately concepts from each other and when aggregate them. For example, the concepts for the terms ”paroxysmal cough” and ”nocturnal cough” can be aggregated into a study of kidney disease, but should be left in a separate study of pneumonia. Determine if two concepts are similar enough to be combined depends on the quantification of the similarity between concepts, resulting in a difficult and context dependent task.

Pivovarov and Elhadad [69] combine ontological approach and corpus, proposing a comprehensive approach that calculates a similarity score for a pair of concepts combining data-driven and ontology-drive knowledge,

demonstrating the method on concepts of SNOMED-CT and on a corpus of clinical notes of patients with chronic kidney disease (based on IDF). Combining the information from usage patterns in clinical notes and the ontological structure, the method can distinguish the concepts that are simply connected by those that are semantically similar.

Melton et al. [70] explores the use of five measures of similarity to determinate the similarity between patients. A database of electronic patient records, including discharge, operative notes of radiology and of pathologies, diagnosis and other information have been made available to experts to manually evaluate documents of similar patients. The authors concluded that the ontological principles and informative content provide useful information for the similarity metrics, but currently do not reach optimal performance because there is no gold standard for determining similarity between documents.

Chapter 3

Fingerprint and Iris based Authentication

As said in paragraph 2.1, in multi-biometric systems based on the matching score fusion level the features vector from each sensor are compared with the respective samples (recorded separately) so that each subsystem can give its own opinion, in the form of points (matching score), which indicates how the features vector is similar to sample [31]. These scores are then combined into a single result which will be forwarded to the supervisor who is responsible of the final decision based on "matching score zone."

Figure 10: Matching score fusion level.

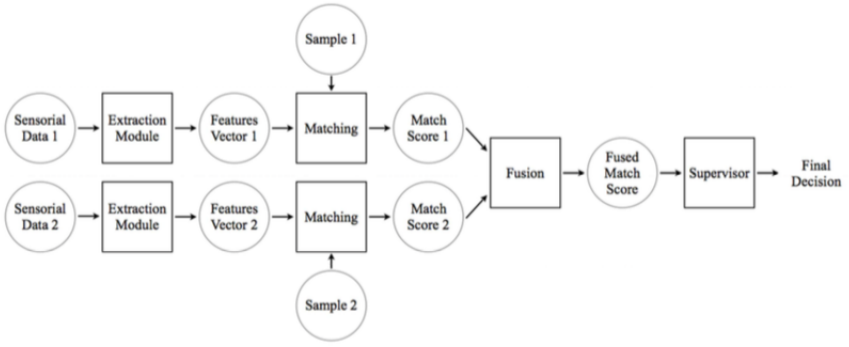

Figure 11: Extraction fusion level.

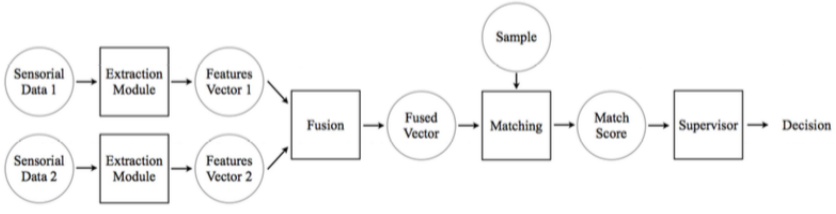

In ranked list combination fusion method (which does not require a normalization process), the list produced by each classifier can be interpreted as the opinion of the classifier itself. In this way, this method can also be seen as a fusion to matching score level (see Figure 10). In the Feature fusion level, the information obtained from each biometric system is successively merged into a single vector. Figure 11 shows this kind of fusion.

Two methods to obtain results are the following:

- Weighted sum: this method can be used only if the features are commensurate; the fusion performs a weighted sum between the various vectors of extracted features from respective sensors;

- Concatenation: it is used in the extraction level fusion where each feature vector is independent from all other (i.e. they are not commensurate as for example a system that works with voice and face). In this case it is possible to concatenate these vectors into a single features vector. The vector thus obtained will represent the identity of a person in a different (and more discriminating) features space.

The homogeneous vector obtained by data extracted is composed by binary sequences representing unimodal biometric models. An header and a biometric template thus compose the resulting vector.

3.1 The Proposed Multimodal Recognition Systems

Many tests to verify performance of the techniques and algorithms above described and exposed have been done. Experimental trials have been carried

out on two recognition systems:

- Multimodal fingerprint/iris recognition system;
- Multimodal fingerprint/fingerprint recognition system.

In what follows, two multimodal recognition systems are analyzed and described. The first one is a fingerprint/iris multimodal recognition system operating in frequency domain. Experimental results are referred to a software implementation. The second one is a fingerprint/fingerprint multimodal recognition system operating in spatial domain. Experimental results are referred to a FPGA hardware implementation.

3.1.1 Fingerprint/Iris Recognition System

The proposed multimodal biometric system is composed of two main stages: the pre-processing stage and the matching stage. Iris and fingerprint images are preprocessed to extract the regions of interest (ROIs), i.e. singularity regions, surrounding some meaningful points.

Figure 12: The proposed Iris/Fingerprint authentication System.

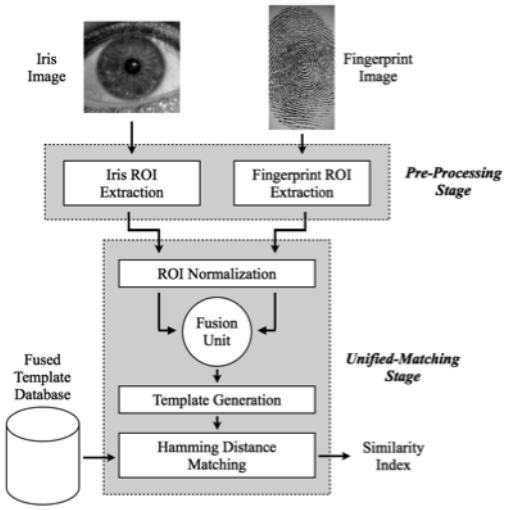

Despite to the classic minutiae-based approach, the fingerprint-singularity-regions-based approach requires a low execution time, since image analysis is based on a few points (core and delta) rather than 30–50 minutiae. Iris image pre-processing is performed extracting the iris region from eye and deleting eyelids and eyelashes. The extracted ROIs are used as input for the matching stage. They are normalized, and then, processed through a frequency-based approach, in order to generate a homogeneous template. A matching algorithm is based on the Hamming Distance (HD) to find the similarity degree.

3.1.2 Fingerprint/Fingerprint Recognition System

An Automatic Fingerprint Authentication System (AFAS) consists of three main processing steps: image acquisition, features extraction, and biometric

templates matching. In the first phase, a sensor scans and acquires the fingerprint image. Successively a vector of features, containing information about the micro and/or the macro features will be extracted. In many cases, this step is preceded by a pre-processing phase in order to enhance fingerprint image quality. Finally, a matching score is used to quantify the similarity degree between the input image and the stored templates. Generally, a threshold based process is used to accept or reject a user. The proposed system architecture is composed of two AFAS modules based on micro and macro features, respectively. Result fusion is realized combining the matching score of both AFASs in order to obtain an overall matching score.

As depicted in Figure 13, the Fingerprint Singularity Points Extraction Module processes an acquired fingerprint image in order to extract useful information (presence, number, and position) on core and delta points. Fingerprint image as well as singularity point information are used as inputs of both Micro-CBA and Macro-CBA Modules.

Figure 13: The proposed Fingerprint/Fingerprint authentication system.

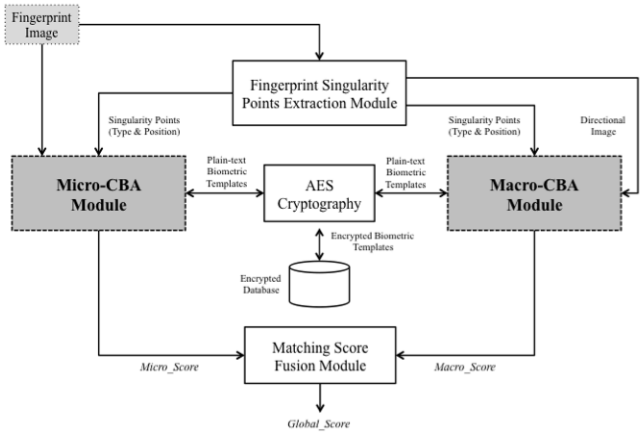

The first one uses singularity point information for fingerprint registration and performs fingerprint templates matching using minutiae type and position (micro-features), while the second one performs fingerprint templates matching using only the directional image of the original finger-print and the singularity points information. Fingerprint templates are encrypted be-fore their storage. The unimodal matching scores are finally combined to obtain the overall matching score. However, singularity point detections can fail, since finger-print could be corrupted, broken or the fingerprint has not core and delta points (i.e. it belongs to the Arch class). In this case, the Micro-CBA Module performs fingerprint templates matching using only minutiae information without fingerprint registration, while the Macro-CBA Module will give zero as matching. For this reason, the overall matching score is obtained using different weights for the two AFASs.

An ideal matching system should be immune to fingerprint translation,

rotation and non-linear deformation issues. For this reason, singularity point information is checked before running the fingerprint matching algorithm. As pointed out before, singularity points presence and position could be used for fingerprint pair registration before evaluating the matching score. However, if no singularity points are extracted, the template matching algorithm will be performed on the set of extracted minutiae without any registration step and fingerprint deformation reduction.

With more details, template matching algorithm is based on extracted micro- features (minutiae spatial coordinates and ridge direction) and involves a fingerprint pair composed by the acquired fingerprint and the stored template. So, the on-line acquired fingerprint image is tentatively registered. Successively, a window, centered in the minutiae position, is considered to reduce deformation problems, when and only when core and delta points are detected.

Finally a comparison between correspondent windows in each fingerprint pair is performed. The Micro_Score will be the percentage of correct matched minutiae.

All the experimental results for both the multimodal biometric recognition systems are discussed in Chapter 7.

Chapter 4

Data Clustering in MRI

MRI is a non-invasive way to quantify the iron overload in various organs [32] through T2* sequences in a non-invasive way, avoiding repeated biopsies.

The purpose of this contribution is to present a novel rapid and non-invasive method, called Liver Iron Overloading MOnitoring Thalassemic (LIOMOT) based on MR images that assess liver iron overload using MRI sequences using three different Regions of Interest (ROI) in the liver to obtain a more accurate measurement of iron overload compared to traditional T2* method avoiding errors caused by heterogeneity in liver iron deposition. Obtained results have been validated using an Expert System (ES) that matches the LIOMOT output with the classification of the state-of-the-art MRI T2* method. The ES validates the results with a great agreement.

4.1 The Proposed Method

The goal of the proposed method is to train an ES for classifying liver iron overloading in thalassemic patients. The ES investigates the use of an Artificial Neural Network (ANN) for mapping a given set of data and for extracting common features and relationships among the data. The mathematical model is trained from an input data set. After the successful training phase, the artificial neural network will be able to perform classification, prediction, or simulation on new data. With more details, the ANN is used for mapping the output of the LIOMOT approach on the output of approach based on

MRI T2* assessment for liver iron overload estimation [33].

The former is a SIR (Signal-to-Interference Ratio) based method for estimating the liver iron overloading in medical examinations based only on image processing techniques.

The latter is based on relaxation time of T2* method in MRI (Magnetic Resonance Imaging) and it can determine the degree of iron overload on human organs such as liver. LIOMOT output is a continue value between 0 and 1, while the MRI T2* output is a classification of liver iron overload. MRI T2* approach classifies the iron overload in four classes: Normal, Mild, Moderate, and Severe. In this way, each entry of the database is composed of a couple of values, i.e. a value between 0 and 1 given by the LIOMOT method, and one of possible classes produced by the MRI T2* technique.

The neural network has been trained using the Levenberg-Marquardt back-propagation algorithm, and it maps the continue value produced by the L.I.O.MO.T method with the four classes produced by the MRI T2* method. The dataset is composed of 200 samples. The 75% of the dataset has been used for the training phase, 20% for the validation phase, while the remaining 5% has been used for the test phase. The selected optimal model has been evaluated considering the Mean Square Error (MSE), and the coefficient of correlation (R), and it shows interesting performances. The dataset used for the training-validation-testing phases is composed of real patients of Hospital "P. Giaccone" located in Palermo, Italy, affected by thalassemia disease. The proposed algorithm has been developed as a plugin for OsiriX, an advanced Open-Source PACS workstation and DICOM viewer [34], using Objective-C as programming language.

4.1.1 The LIOMOT Approach

Liver Iron Overloading MOnitoring Thalassemic patients is a Signal-to-Interference Ratio method [35][36]. It can be considered a non-invasive assessment done by MR imaging. In SIR methods, the signal intensity of a target organ is correlated with the signal intensity of a reference tissue (e.g. fat, or muscle). In LIOMOT approach, MR imaging was performed with the following key settings, as shown in Table 1:

Table 1: Parameters of M.R. Imaging.

Series	# of Slices	Slice Thickness (mm)	TR (ms)	TE (ms)
Axial T2* G.R.E.	11	5	225	3

Despite to the traditionally T2* relaxant methods, the LIOMOT method requires only one acquisition. On the other hand, MR images denotes high sensitivity to iron burden in the organ.

The paravertebral muscles are used as referenced tissues, since they combine good sensitivity with low intensity variability. The LIOMOT produces an output value between 0 and 1 that estimates the presence of iron in liver. Values close to 1 indicate a low presence of iron, while values close to 0 indicate an high iron level [37].

4.1.2 MRI T2* Assessment for Liver Iron Concentration

Liver Iron Concentration can predict a clinical outcome, such as patients with less LIC survive longer and have less cardiac diseases. LIC level assessment can be taken by biopsy and MRI. Assessment of iron overload is

based on T2* relaxation time decrease induced in the liver due to the paramagnetic properties of iron. This acceleration of the T2* relaxation time is proportional to the quantity of iron and leads to a decrease in the MRI signal intensity from the liver. In [38] the T2* labels the presence of iron in liver in four classes: Normal (T2* $>$ 11.4 ms), Mild (T2* 3.8 - 11.4 ms), Moderate (T2* 1.8 - 3.8 ms), and Severe (T2* $<$ 1.8 ms), as shown in Table 2:

Table 2: Correlation between iron overload detected by Magnetic Resonance Imaging (ms) and Tissue (mg fe/g dry weight).

Liver	Normal	Mild	Moderate	Severe
T2* (ms)	$>$ 11.4	3.8 - 11.4	1.8 - 3.8	$<$ 1.8
LIC (mg FE/g)	$<$ 2	2 - 7	7 - 15	$>$ 15

4.2 The Proposed Neural Network Model

We consider feed- forward neural networks, and the back-propagation learning algorithm will be used to train the ANN. In this work a neural network for developing a Medical Expert System is proposed. The ANN is useful for classifying liver iron overloading in thalassemic patients.

Figure 14: The structure of the ANN.

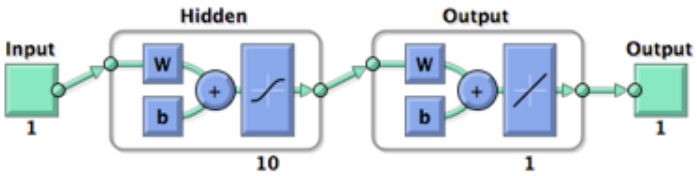

As explained above, the MRI T2* approach classifies the presence of iron in liver in four classes: normal overloading, mild overloading, moderate overloading, and severe overloading, while the LIOMOT approach computes a continue value between 0 and 1 for estimating the presence of iron in liver. The proposed ANN is composed of 10 hidden neurons and 1 output neuron (see Figure 14). The kernel function of hidden neurons is the sigmoid function, while the kernel function of output layer is the linear function. The training set is composed of a vector of pairs. The former is the output of the LIOMOT method, and it is used as input for the ANN. The latter is a class of MRI T2* method and it is used as ANN's target. The ANN is trained using Levenberg-Marquardt Back-Propagation algorithm, considering the maximum limit of 100 epochs.

The dataset is composed by 200 samples, both LIOMOT evaluation and MRI T2* evaluation were acquired by three expert physician. The dataset was divided in three bins for creating the training (75%), validation (20%) and test (5%) sub-datasets. The Experimental Results are discussed in Chapter 6.

4.2.1 OsiriX Plugin Implementation

The proposed method has been implemented as plugin for OsiriX (see paragraph 1.3), an advanced open-source PACS workstation and Dicom viewer [39]. The language used is Objective-C. The images can be produced by several imaging equipment as MRI, CT, PET, PET-CT, etc. An OsiriX advantage is to permit the development of ad-hoc plugins for particular physicians' requests. Figure 15 shows the plugin GUI developed for liver iron overload

estimation in thalassemic patients. To use the plugin, the physician initially selects four regions of interest. The ROIs have a circular shape and a fixed surface of 0.3 cm^3. The ROIs are selected in order to identify the right lobe, the left lobe, and the paravertebral space of the liver, while the last ROI is the referenced tissue, and it is selected on the paravertebral muscle.

Figure 15: The developed OsiriX LIOMOT plugin. The Gui shows the output after iron overload estimation.

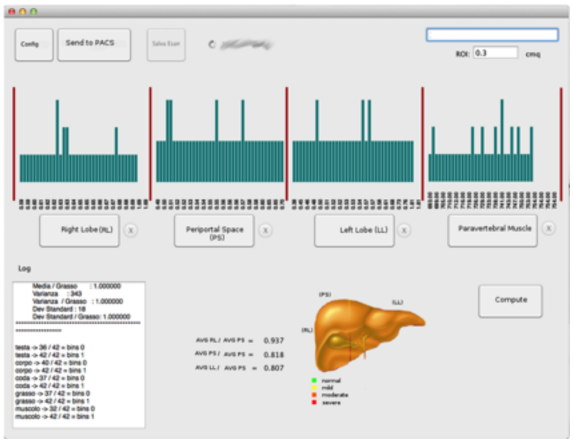

The output of the plugin shows the class of the liver iron overload according to the four MRI T2* classification: normal, mild, moderate, and severe overloading. The normal class of iron overloading is represented with the green color, mild class with the yellow color, moderate with the orange color, and the severe class with the red color. In the above figure is shown the output of the computation. On the left, the GUI shows the Log output that inform the user about computational steps; in the central area, the numeric values of the iron overload assessment are represented. On the right, the GUI shows a graphical and colored representation of the liver.

In this example the liver has a mild liver iron overloading, and it is highlighted in yellow color. The proposed framework is useful for a clinical practice. It is exploited for estimating the sizing of the chelation drugs based therapy in order to control iron overloading in thalassemic patients.

Experimental results and results will be investigated in Chapter 7.

Chapter 5

Thermometry in MRI

Hyperthermia is a type of clinical treatment in which body tissues are exposed to high temperatures that can kill pathological lesion, like uterine fibroids [39] In MRgFUS treatments [40], [41], high temperatures are applied on local and small areas by using ultrasound beams that deliver energy to heat the tumour. MRgFUS treatment is performed using the ExAblate 2100 equipment (InSightec, Haifa, Israel), integrated with a Signa HTxt MR scanner (GE Medical Systems, Milwaukee, WI). Thermal ablation of fibroids tissue is done using sonication process: the tissue is heated with Focused UltraSound concentrating a high-energy beam on a specific point. This allows to reach a temperature higher than 50°C causing proteins coagulation and consequently inducing the fibroid tissue necrosis.

The planning, treatment and evaluation processes are possible thanks to MR Imaging (MRI) guidance, which can also be used to reconstruct maps of tissues temperature. This makes it particularly enabling for guiding and monitoring thermal therapies.

5.1 The Proposed Interpolation Model

In a MRgFUS treatment, a little area of the patient's organ is heated by a focused ultrasound beam, increasing temperature in that point. The process is repeated several times until the whole lesion area is treated.

Figure 16: 3D plot of temperature map after 5 seconds treatment; a) the maximum temperature reached in the peak is about 52°C. b) the temperature map after 15 seconds of sonication; c) the temperature map after 30 seconds of sonication. The temperature peak is 87°C.

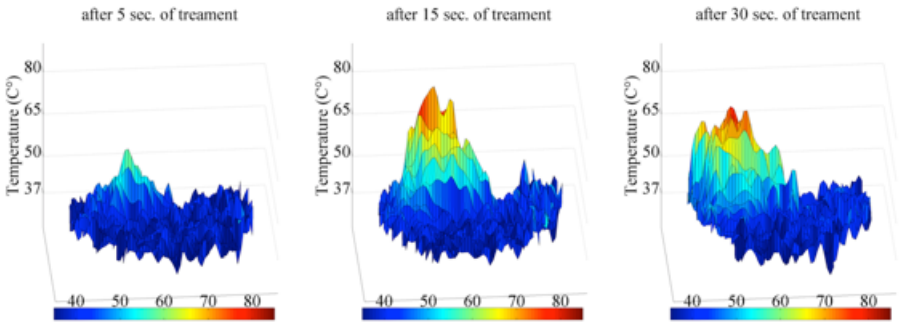

In Figure 16 it is possible to see a sequence of temperature maps: the sonication burst takes about 30 second for each sonication, and the number of sonications are related to position, type, and size of uterus fibroid.

In referenceless phase estimation, a Region Of Interest (ROI) is selected around the area to be heated. First of all, to perform interpolation it is necessary to select two regions (outer and inner) in the phase image. Figure 17.a shows the inner ROI containing the heated region, surrounded by baseline (outer) region. In the proposed approach, it is possible to choose an inner ROI with any shape, while generally other algorithms use only circular or rectangular shapes. The choice of an arbitrary shape leads to an accurate isolation of the heating region allowing us to use real baseline data (Figure 17.c). It is essential to choose the outer ROI outside the heated region because temperature changes within the frame ROI will affect the reconstruction of the background phase.

As said before, one approach to this problem is to fit the data with a polynomial function. However, an invertible system that uniquely de-

fines the interpolant is not guaranteed for all positions of the interpolation points. Moreover, such a polynomial interpolant will typically display spurious bumps and wiggles.

Figure 17: a) Inner selected ROI in the phase image (with the typical cigar-shape); b) 3D plot of sonicated area (a); c) Result of sonicated area removal.

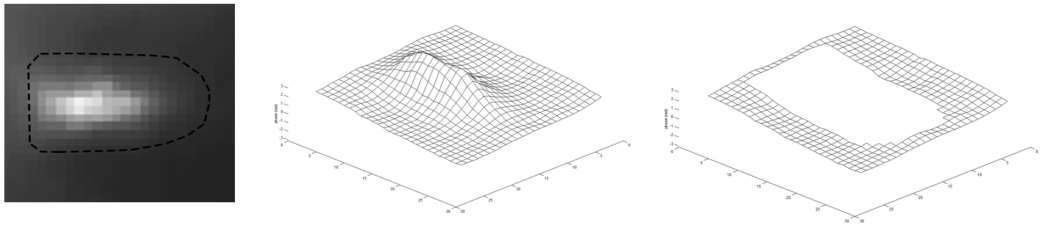

a) b) c)

In this work we propose a model that reconstruct background phase in the frame ROI using a Radial Basis Function (RBF) neural network [42], [43]. RBF approximation method offers several advantages over polynomial interpolants:

- the geometry of the known points is not restricted to a regular grid and there is no need to define a mesh of patches;
- the resulting system of linear equations is guaranteed to be invertible under very mild conditions;
- polyharmonic RBFs have variational characterizations, which make them eminently suited to interpolation of scattered data, even with large areas of missing data.

5.1.1 Radial Basis Function Approximation

We begin by introducing radial basis function approximation generally before considering the specific case of approximating as a function of two variables. Consider $f : R^d \rightarrow R$ a real valued function of d variables that is to be approximated by $s : R^d \rightarrow R$, given the values $f(X_i) : i = 1, 2, \ldots, n$, where $X_i : i = 1, 2, \ldots, n$ is a set of distinct points in R^dcalled the interpolation nodes. We will consider approximation of the form (6):

$$s(X) = p_m(X) + \sum_{i=1}^{n} \lambda_i \phi(\|X - X_i\|), X \in R^d, \lambda_i \in R \tag{6}$$

where is a low-degree polynomial, or is not present, denotes the Euclidean norm. Thus, the radial basis function s is a linear combination of translations of the single radially symmetric function, plus a low-degree polynomial. We will denote with the space of all polynomials of degree m at most in d variables. Then the coefficients of the approximation s are determined by requiring that s satisfies the interpolation conditions expressed in the following equation:

$$s(X_j) = f(X_j), j = 1, 2, ..., n \tag{7}$$

together with the side conditions:

$$\sum_{i=1}^{n} \lambda_i q(X_j) = 0, \forall q \in \pi_m^d \tag{8}$$

Some examples of popular choices of ϕ and the corresponding radial function are given below:

$$\begin{cases} \phi(r) = r & linear \\ \phi(r) = r^2 \log r & thin - plate - spline \\ \phi(r) = e^{-ar} & gaussian \\ \phi(r) = (r^2 + c^2)^{1/2} & multiquadratic \end{cases}, r \geqslant 0$$

where a and c are positive constants. Some typical conditions on the nodes under which the interpolation conditions (7) and (8) uniquely specify the radial basis function (6) are given in Table 3. In this context "not coplanar" means that the nodes do not all lie in a single hyper-plane, or equivalently that no linear polynomial in d-variables vanishes at all of the nodes. The surveys of Powell [44] and Light [45] are excellent references for these and other properties of radial basis functions.

Table 3: Conditions imposed on nodes for various Radial Basis interpolants.

Function ϕ	spatial dimension d	polinomial degree m	restriction on nodes
Linear	any	1	not coplanar
Thin-Plate	2	1	not coplanar
Gaussian	any	absent	none
Multi-quadratic	any	absent	none

In this paper we are particularly concerned with 2D (depth-map) data and will consider linear, thin-plate spline and multiquadratic interpolants. Then equations (7) and (8) imply that the coefficients of the radial basis function and the polynomial can be found by solving the linear system:

$$Q = \begin{bmatrix} 1 & x_1 & y_1 \\ 1 & x_2 & y_2 \\ \vdots & \vdots & \vdots \\ 1 & x_n & y_n \end{bmatrix} \tag{9}$$

$$\lambda = (\lambda_1, \lambda_2, \ldots, \lambda_n)^T \tag{10}$$

$$c = (c_0, c_1, c_2)^T \tag{11}$$

$$p_1(x) = c_0 + c_1 x + c_2 y \tag{12}$$

$$f = (f_1, f_2, \ldots, f_n)^T \tag{13}$$

The thin-plate, or 2D bi-harmonic spline we consider models the deflection of an infinite thin plate. While the linear radial basis function will interpolate the data, the thin plate spline is more attractive since it also provides C_1 continuity and minimizes the energy functional, expressed by equation (14), over all interpolants for which the energy functional is well defined.

$$E(s) = \int (\frac{\delta^2 s}{\delta x^2})^2 + 2(\frac{\delta^2 s}{\delta x \delta y})^2 + (\frac{\delta^2 s}{\delta y^2})^2 dxdy \tag{14}$$

In this sense the thin-plate spline is the smoothest interpolator of f. Higher-order polyharmonic splines achieve continuity of higher derivatives.

5.2 The Proposed Referenceless Thermometry Method

After outer and inner ROIs selection, we obtain an image with data in outer ROI, and no values in the inner ROI. The goal of referenceless thermometry is to obtain reconstruction of inner ROI, in order to have an estimated baseline image to subtract from current image that we are evaluating, obtaining a temperature rise caused by thermal ablation.

The first task is to calculate the coefficients of interpolant function. In our solution, the used procedure is as follows. The nodes are first scaled uniformly in x and y, and shifted so that the new nodes lie in the unit square. Subsequently the interpolation problem, corresponding to the transformed data, is solved using the double-precision diagonal pivoting method for symmetric indefinite systems from Lapack. The interpolant was compared with the original baseline image. The natural criterion for assessing a reconstructed phase image is how closely it matches the baseline surface prior to the removal of the heated area.

The interpolant fitted to the incomplete depth-map was then compared with the original baseline surface.

Firstly, it is selected the temporal instant with the maximum temperature rise, in order to obtain the biggest possible mask to crop sonications in the series. Before performing the calculations, wraps present in the phase image are unwrapped using the use of Goldstein, Zebker, and Werner's algorithm [46].

After phase unwrapping, a part of the phase image is individuated, selecting 2 ROIs: the first one, rectangular, contains a sufficient number of

phase data of a constant region; the second one, that have an arbitrary shape surrounds the heated region clipping phase variation data, that leads to wrong phase estimation. The result is a mask that will be applied to each phase image of the entire series, in order to crop each phase image.

Each outer ROI, where the inner ROI has been reconstructed using RBF interpolation, represents the baseline data for each temporal instant. We reconstruct the inner region in four different ways:

- interpolating data with a 5° order polynomial , as well as done in [47];
- interpolating data with Linear RBF;
- interpolating data with Thin-Plate Spline RBF;
- interpolating data with Multiquadratic RBF.

Figure 18: The structure of a neural network implementing the RBFs as hidden layer.

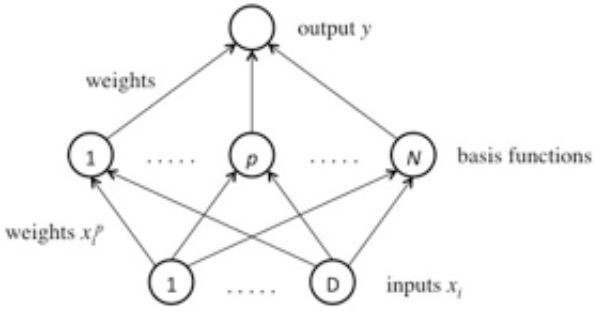

The RBF network is composed of two layers, and the N training patterns x_i^p, t^p determine the weights directly. The hidden layer multiplies the activation units as shown in Figure 18.

After the interpolation, we calculate temperature rise obtained for each type of interpolation, using Equation (5) and using a different estimation of baseline ($\phi(T_0)$) phase image. Each temperature rise is then compared with PRF shift thermometry that is used as our gold-standard. Interpolation results are shown in Figure 19.

Figure 19: a) 3D plot of baseline phase with no heating; b) The same region after 20s treatment; c) Removal of sonicated area; d) RBF reconstruction of phase map of the image in c); e) Difference between RBF reconstruction (d) and original baseline (a).

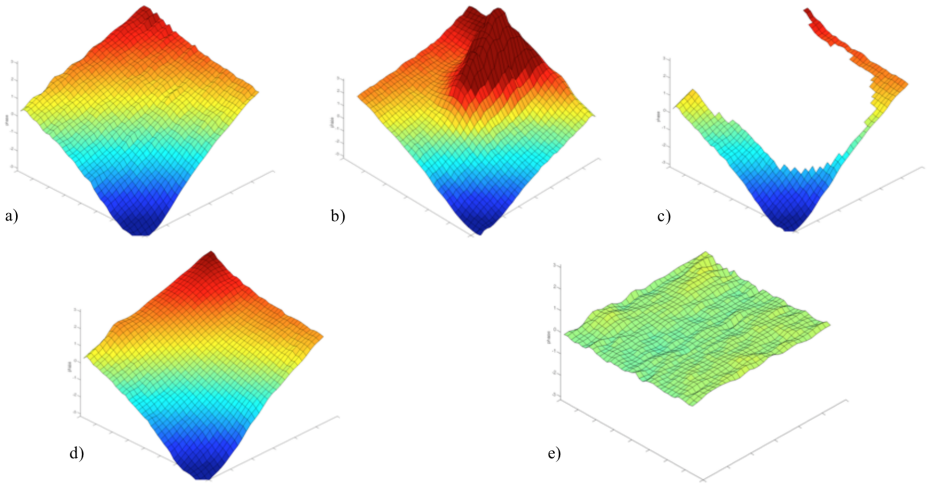

The workflow of the proposed method for enhancing the referenceless thermometry by using RBF interpolation has been implemented as follows:

1. once the series of images is acquired, we recover the original phase from the 2π-wrapped phase images by using the Goldstein, Zebker and Werner's algorithm;

2. the RBF artificial neural network takes input data from the region between the sonicated area and the uterine contour;

3. the area to be reconstructed is iteratively interpolated by using RBF, which represents a practical solution for the problem of interpolating incomplete three-dimensional surfaces. The implementation of the reconstruction algorithm invokes iterative refinement to improve the accuracy of the solution;

4. for each temporal instant the extrapolated baseline phase that is used together with the global (currently heated) image.

Figure 20: The workflow of the proposed method.

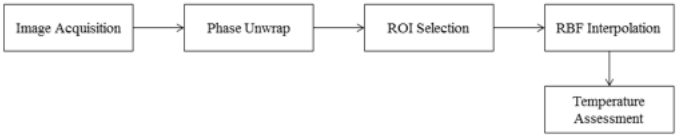

Results and discussions for the novel thermometry method, evaluated on two different datasets, will be shown in Chapter 7.

Chapter 6

Image Segmentation in CT and MRI

In the following Chapter, two segmentation method are proposed. The first one segments CT hepatic lesions for a follow-up assessment of a pharmacological cure; the second one quantifies the CSF, GM and WM of a MRI T1volumetric 3D brain datasets, comparing the segmentation results with the results of a famous used VBM software on the same dataset.

6.1 Liver Lesions Segmentation

Hepatic metastases are the most diffused secondary lesions in patients with primitive colon and gastrointestinal stromal tumor (GIST). Recently, optimal antitumor effects have been reached through molecules target dosing, such as multi-kinase inhibitors that inhibits oncogenic kinases, angiogenesis and stroma.

After the introduction of these target molecules, there has been a growing concern about the usage of the traditional criteria of tumor response; Infact, the objective assessment of tumor response became increasingly important with rapid and continuos development of these new drugs.

The first guidelines to evaluate the response criteria tumor, stipulated from OMS at the beginning of 1980, were based on the size of the lesions determined from the sum of the products of 2D measurements. Since their introduction, these guidelines were further simplified so 1D measurement of the lesions could be used. These criteria were successively validated by RE-

CIST group, according with the guidelines stipulated from OMS. However, these criteria based only on measurements of 1D or 2D lesions, do not directly reflect the biological changes that occur after the administering of such molecules. In addition, patients in advanced disease stages necessarily don't present an increase in the size of the lesion or the appearance of new lesions, but may present a new phenomenon called lump-mass. All these features are not addressed by the RECIST criteria, which are based exclusively on the measurement of diameter axial lesions. In fact the radiological changes induced by such drugs are heterogeneous: in particular, these target therapies not only induce changes in lesion's size but also in the structure, often causing a decrease in density, emphasizing intra-tumoral nodules and tumor vasculature, with subsequent size reduction.

Recently a turning point occurred with the use of Choi criteria that simultaneously evaluates dimensional and densitometric criterias and subsequently biological response.

Such responses are analyzed by examination by computerized tomography (CT) after medium contrast, which has been shown to be very sensitive in the study of intestinal wall and for early detection of liver metastases.

Here, the necessity to study and develop a methodology that can segment liver lesion regions, allowing the calculation of values such as tissues density, variance, area, transverse diameter, volume, and 3D reconstruction for a better evaluation from the anatomical point of view.

6.1.1 The Proposed Multi-Seed Region Growing Segmentation Method

The images in question are in DICOM format and come directly from a CT scanner with 64 detector rows. To enable better accuracy of the segmentation, the images are initially pre-processed to reduce noise through the use of smoothing filters [48] [49].

The liver injury in this type of images are characterized by radio-densimetric values attributable to aqueous tissues (hypodense lesions), different from the values belonging to a healthy liver, so the chosen segmentation method belongs to region growing algorithms.

The aforesaid algorithms grouping the pixels or sub-regions in gradually larger regions based on predefined criteria. An algorithm of this type bases its operation on the difference of the pixel values: starting from a seed region, composed of one or more pixels interior to the object to be segmented, evaluates the neighboring pixels to determine whether they should be considered part of the object, and if so they are added to the region. The growing process continues until there will be pixel to retent in the region, until a stop condition is reached.

The evaluation criteria of the pixels typically depends from their Hounsfield value, from the type of connectivity used to determine the neighbors and from the strategy used to visit the neighboring pixels. A simple but effective criterion to include pixels for region growing is to assess whether the intensity of the pixels falls in a specific range. In hepatic injury is seen that, as they are of hypodense type, the Hounsifield average value is around 0, with values typically falling in the range (-50, 50).

The segmentation software requires two operator input: a starting point inside the lesion, which will be the seed of the region, and the range of values which generally will be part of the lesion. The operator, by clicking on a point of injury through mouse, set the span manually from the keyboard or rule this interval via a slider. Once obtained input, the region growing algorithm iterates and assesses both the pixels in the same slice of the seed point, and also in depth and evaluating the subsequent and previous slices to the current one (3D segmentation).

6.1.2 OsiriX Plugin Implementation

It has chosen to implement the proposed software form plug-in for the popular open-source software OsiriX.

Figure 21: The developed plug-in for OsiriX Dicom Viewer.

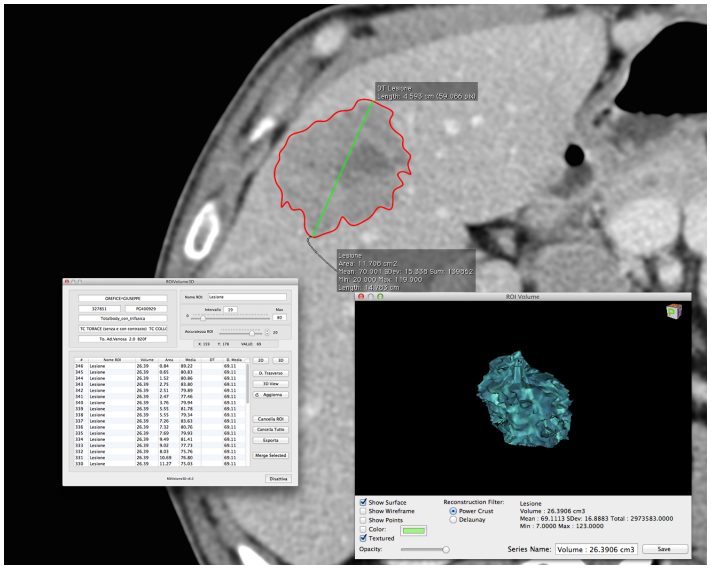

Such choice is justified by the reliability and robustness of OsiriX libraries used by, for example, the Insight Toolkit (ITK), which implement algorithms robust and tested for the Segmentation of medical images.

6.2 Voxel Based Morphometry

The need to evaluate the brain volumetry using quantitative studies is now predominant in neuroscience field. Using the most advanced MRI techniques, we are able today to study many neurological disorders in degenerative diseases associated with dementia, in which the neuronal depletion results in "atrophy", accompanied by volumetric reduction of white's and grey's matter. The consequences of these reduction, characteristic of almost all forms of primary and secondary demential syndromes, can be assessed through semi-automatic analysis software that can identify and quantify the different intracranial compartments tissues such as grey matter (GM), white matter (WM) and cerebrospinal fluid (CSF).

The Voxel-Based Morphometry (VBM) is an analysis technique based on segmentation of medical images able of perform a characterization of the brain's neuro-anatomy; datasets are split into their constituent parts. This characterization is based on the intensity of the signal, usually weighted in MRI T1 or T2 sequences, in different tissue compartments. The aim of the VBM is to determine if a specific voxel has different intensity in one group instead to another. The VBM correlates morfovolumetric variations with the variation of strict parameters, allowing for example to compare results between pathological subjects and healthy controls (comparison between groups) or longitudinal comparisons (in follow-up) in the same patient

or patient groups.

Today several software allows the estimation of the VBM using different techniques:

- FMRIB Software Library (FSL) [51] is a software developed by the Center of Functional MRI Oxford University consists of programs for analysis and statistical analysis of neuroradiological images. This software, in reference to the techniques of VBM, mainly consists of three components: BET, FAST and FLIRT. The FMRIB's FSL is a tool that allows many studies, and in particular FAST software is the segmentation algorithm of FSL that allows the classification of the three major cerebral tissues: white matter, gray matter, cerebrospinal fluid. The method is based on Hidden Markov Random Field (HMRF) model associated with an algorithm of Expectation-Maximization, which maximizes the posterior probability and labels the segmented tissues. The process, for a typical volume of 120 slice of about 1 mm thick, with a matrix of 256x256 pixels, takes about 15 minutes in most modern computer;

- Statistical Parameter Mapping (SPM) [52] is an open source tool for the segmentation in Matlab, which uses both functional and structural statistical methods of analysis of neuro-images, that can provide a probabilistic classification of the brain tissues in MRI images, increasing the precision of each tissue class. The used algorithm is the voxel-based morphometry (VBM), that consists in an initial spatial normalization, the segmentation in the respective classes of tissues, in

smoothing and in the use of a prior to compute the statistical probability of membership of each voxel to each class. A-priori probabilistic maps are also used, which combined with the intensity of each voxel through the Bayes rule, return the probability a-posteriori. SPM joins the theories of general linear model (GLM) and the Gaussian random field (GRF) to analyze and inference indirect spatial data through statistical parametric maps.

These software applications have their limitations: the high number of parameters to be set, from which follow a more or less correct segmentation, and the times of segmentation very high (typically from 15 to 30 minutes).

The aim of this contribution is to present a brain segmentation system, that take in input a whole 3D T1 brain dataset, and segments the volume in the three main brain's matter: WM, GM and CSF. The advantage of the method is the totally operator's independency (parameters-free), and the speed of execution of the entire algorithm, if compared with the most used VBM software.

The segmentation method relies on a k-means clustering and an artificial neural network (ANN) classifier. The segmentation results have been compared with the results obtained from the FSL segmentation, obtaining great results. The dataset used for algorithm development, testing, and comparison with the other software is the Internet Brain Segmentation Repository (IBSR) [51], that provides manually-guided expert segmentation results along with magnetic resonance brain image data, containing the datasets of 18 T1-weighted MR acquisitions of its patients, and segmentations per-

formed manually by experienced radiologists in three different tissues: WM, GM, CSF.

6.2.1 The Proposed Segmentation Method

The proposed system is able to segment a T1-weighted MRI brain acquisition in White, Gray and CSF matter [55]. The method is totally automatic: in input a T1 sequence is requested, and the algorithm produces the requested segmented tissues in output. The dataset is often composed of several hundreds of slices, with resolution of 256x256 pixels. The workflow of the proposed system is composed of the following steps:

1. each brain slice is clustered in 3 tissues using a simple k-means algorithm;

2. the output of the k-means will be the training set of the ANN;

3. the trained ANN receives the original brain dataset as input, and gives in output three values, each one belonging to White, Gray and CSF matter.

The system is divided in two phases: a training phase, and a segmentation phase. The training phase classifies the input dataset by using k-means algorithm; each slices is classified in six clusters, and the clusters are aggregated in three clusters by sorting them using the mean value of each cluster. The feed-forward neural network is composed of 30 neurons in the hidden layer, and 3 neurons for the output layer. The 30 neuron value has been chosen after several trials on the whole dataset. The NN takes the output of k-means

clustering as input for the training phase: after 50-100 iterations the MSE converges and the training phase has terminated.

6.2.2 K-Means Classification Module

Is the function that performs the classification of brain tissue in the white matter, gray matter and cerebro-spinal fluid, which constitute the target set for the neural network training. This module takes as input the T1 volume and makes an unsupervised classification using a classical K-means clustering algorithm. The k-means is configured with three classes: the algorithm aims to partition all the given voxels into k clusters, in which each voxel belongs to the cluster with the nearest mean, serving as a prototype of the cluster.

From experimental results, the direct classification into 3 classes of the brain volume provides poor results because the brain is not exclusively composed of three distinct tissues, but there are intermediate transition zones. These regions have not a net area of demarcation between different tissues, indeed lead to an incorrect recognition of the contours, and then to an incorrect tissues segmentation.

Figure 22: The 6-class k-means voxel clustering.

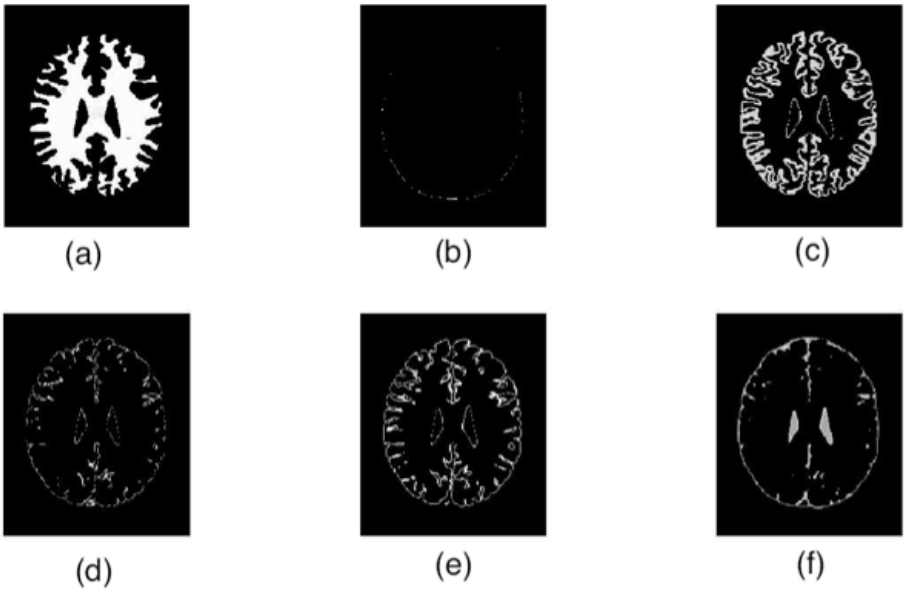

To overcome this problem, it was decided to classify the voxels of the brain volume in six different classes, performing a downstream merger of the intermediate classes with the correct classes WM, GM and CSF. The segmentation in six classes then takes into account the following regions:

1. CSF: the region in where there is presence of cerebrospinal fluid;
2. CSF / GM: mixed region with presence of cerebrospinal fluid and gray matter;
3. GM: region with the prevailing presence of gray matter;
4. GM / WM: mixed region with presence of white matter and gray matter;

5. WM: region with the prevailing presence of white matter;

6. Background: brain areas outside the region.

The intensity values of the gray scale MR images are directly related to the type of brain tissue. For example, on T1 a high intensity value identifies white matter, a intermediate value is the gray matter, and a low intensity value is related to cerebrospinal fluid. In the transition's regions we have intermediate intensity values that identifies however the prevalence of WM, GM, or CSF, which will be reordered in function of the average intensity value. The classes are then unified in adjacent pairs based on the smaller difference of in-tensity by reducing the number of classes from 6 to 3.

By applying this procedure, we can obtain a significant improvement in the classification of brain images through K-means in the white matter (WM), gray matter (GM) and cerebrospinal fluid (CSF), significantly reducing the presence of artifacts introduced by a misclassification.

6.2.3 Neural Network Training Module

At the end of the segmentation phase, performed by the K-means module, the next step consists in the neural network training phase. The training is performed taking as inputs the T1 MRI sequence and the obtained voxel classification of the K-means module.

Figure 23: The implemented Neural Network classifier.

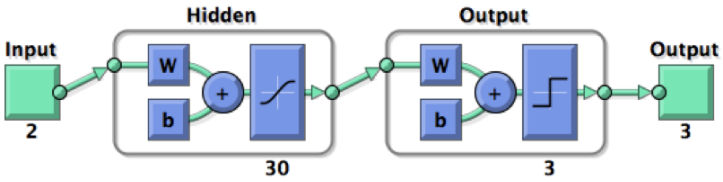

The artificial neural network is of a feed-forward typology, and it consists of two layers. The back-propagation error algorithm allows to train the network starting from a training set composed of the set of inputs and the target set. The neural network is trained to perform the classification of patterns through the back-propagation algorithm, known as gradient descent. This algorithm moves the weights in the direction of the negative gradient, i.e. in the direction in which the performance function decreases more rapidly. The training process will end when performances reach a smaller value of goals, or when the gradient of the performance is below the minimum threshold value.

At the end of the training phase, the neural network can classify sequences provided in input. Once that the NN segmentation tool is ready, is possible to put the brain dataset in input and use the NN for the segmentation purpose. After a quick elaboration phase, the output of the NN is a logical volume, where each voxel belongs to White matter, Gray Matter, CSF fluid or nothing.

6.2.4 Neural Network Classification Module

The segmentation is performed by the neural network, which classifies brain tissues in the three desired classes. The input of the neural network is a

T1 brain dataset; every slice is processed by the NN and at the end of the process, each voxel will be labeled in one of the 4 possible values: 0 (background), 1 (CSF), 2 (gray matter), 3 (white matter). The final step is to unify and label the result of the classification in one image. By iterating this process for each image in the sequence we will get the whole segmented brain volume.

Results, comparison with FSL segmentation results, and discussion are explained in Chapter 7.

Chapter 7

Mammographic Reports Retrieval and Classification

In the medical field it is useful to the comparison of the reports with the presence of multiple clinical concepts, but until now, research has focused on the control of the similarity between individual concepts. We propose an extension to the calculation of the cosine to compare the similarity of the considered reports, that exploit the text pre-processing and the knowledge modeled by radiological ontology, and add relations "is-a" and "Equivalent-to", that show improvement if compared to both the simple matching techniques, such as lexical comparisons based on the Levenshtein distance, and both of the simple calculation of the same cosine [72]. The dataset is composed of 126 reports.

7.1 Mammographic Reports Dataset

Reports were randomly extracted from a mammographic reports database of patients of the Radiological Information System of the University of Palermo Policlinico Hospital, and classified by three expert radiologists in 12 categories.

7.2 The Proposed Ontology-Based Retrieval System

The reports have been classified by the proposed classification method, and by a classification method based on Levenshtein distance and K-Means. We have calculated the of sensitivity and specificity indexes in order to evaluate

the goodness of the proposed classification method.

The system architecture is shown in Figure 24.

Figure 24: The proposed system architecture.

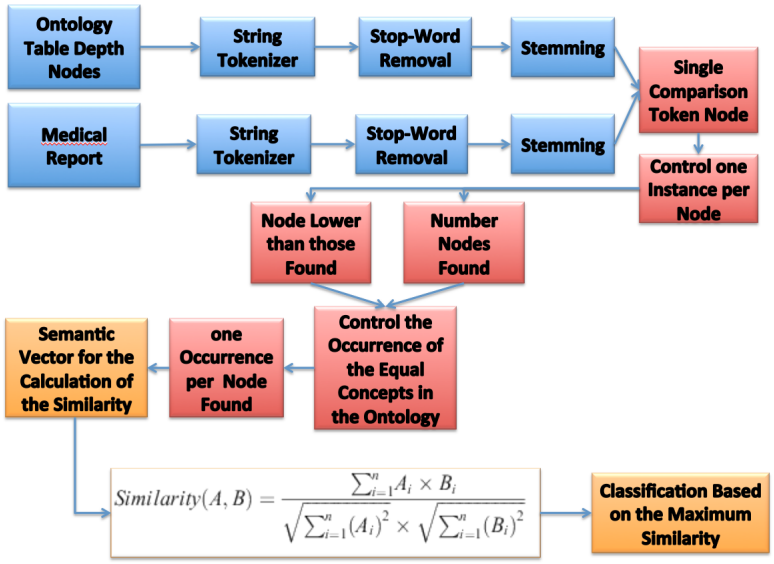

The free text medical reports and all nodes-concepts present in the ontology are pre-processed through four phases, identified as blue rectangles. This phase is required to reduce and standardize medical terms and to improve the results of the information retrieval process. After the pre-processing step, each report is compared with all of the ontology concepts, identified as red rectangles. In our proposed system each report is represented by a N- dimensional semantic vector, where N is equal to the number of ontology concepts, with the introduction of the concepts of "is-a" and "equivalent-to", identified as orange rectangles. In this way the carriers, in addition to having the elements of value 1 (present) or 0 (not present), may have not-orthogonal concepts that are proportional to the depth of the possible common ances-

tor. The input of the system is a specific medical report, and the comparison process with all reports is executed. The outputs of the system are all the reports with maximum similarity. The steps of the proposed method are the following:

Ontology and Table Depth Nodes

The ontology describes the semantic similarity as the similarity between concepts representing report to compare. It represents a source of knowledge where medical terms are organized and where it is possible to assess relationships between concepts. The ontology is composed of 731 concepts, or nodes, and the maximum depth of the hierarchy tree is six. All the concepts have been written in collaboration with three expert radiologists skilled in breast imaging. Based on ontology a table that contains the depth of each node within the ontological tree starting from the root has been created.

String Tokenization (Sentences Identification)

In this phase, each real clinical report is transformed in a flow of significant words (tokens) from which stop-words are removed (terms with low significance, such as prepositions, auxiliary verbs and other words commonly used). Words can be easily identified by the presence of spaces, line breaks, and punctuation marks. Once all special characters are removed (_ <> : , . ; ! ? / & $ ^ ' \T \r) and a process of tokenization that recognises the "Single Words" is done, a flow of significant words on which be able to work is obtained.

Stop-Word Removal

The purpose of this step is to identify the meaning of the whole sentence, starting from the meaning of each term, and the relationships between them.

The meaning of a sentence is not only given by the words contained, but also on the knowledge of the rules for the construction of a sentence in a given language. The combination of words, the order in which they appear in the sentence, and the links bind the words with other words determining the meaning of the sentence [13-15]. Highly frequent terms highlight the words with low discriminatory power, including prepositions, auxiliary verbs and other words in common use: the elimination of these Stop- Words allow the reduction of 30-50% of the used terms.

Stemming

Stemming phase is a reduction procedure of all the words that have the same root, the stem. The procedure is then applied in order to remove words suffixes and extract stems. Words that begin with the same character set or have a sequence of characters in common may have the same etymological origin and similar information content. Generally, this procedure removes the ends of words, leaving a common stem. Because of its high efficiency, the Italian version of the Porter algorithm [71] is used in this work. The algorithm reduces inflections and sometimes the words derived stem or the shape of the root.

7.2.1 Semantic Vector for Similarity Calculation

To overcome the limitations imposed by the direct combination that requires the presence of the same exact concepts in both compared reports, in this study we use the semantic similarity. If we consider, for example, the concept of "fibroadenoma" extracted from the first report and the concept of "benign alterations" extracted from the second report, with a direct comparison

based on the limited syntax for keywords on the reports, and not taking into consideration that the same word may have a different meaning depending on the context in which it appears, there would be no relationship between the two reports because there are no common concepts. Actually, fibroadenoma is a specialized form of the most common benign breast alteration and is more common in women under the age of thirty. Whereas the analysis based on the semantics does not just search for the words on the score sheet but makes contextualization, making analysis dependent from hierarchical ontology that structures from relational point of view, there is a need to take into account the semantic relationships between these concepts to calculate a similarity, like an experienced physician correlates reports based on his background knowledge on relations between concepts. In this study, we use the is-a relationship ("fibroadenoma", i.e. "fibroadenoma", is a kind of "benign alterations", i.e. "alterazione benigna") and equivalent-to ("heterogeneous absence", i.e. "assenza eteroformativa", is equivalent to "heteroplastic absence", i.e. "assenza eteroplasica"), which binds the concepts in reference ontology. The number of these links is understood as the degree of semantic similarity between concepts of interest. More distant are two concepts in the hierarchical representation of the ontology, than lower the similarity because inversely proportional to the distance between the concepts, and more precisely defined as [64,65]:

$$Similarity(Concept1, Concept2) = \frac{1}{path} \tag{15}$$

where path is the number of nodes on the shortest path between the two concepts $Concept1$ and $Concept2$ (15). The goal of the proposed method is to determine the similarity between two clinical reports that contain generally more breast concepts. A standard approach to compare the similarity of reports used in the vector space model is to calculate the cosine between two vectors [67]. The cosine similarity is a heuristic technique for measuring the similarity between two vectors generally used for the comparison of texts in Data-mining and text analysis.

In the analysis of the texts, you will get the values 0 and 1, where 1 indicates that the same words are present in the two texts and 0 that the word is not present in both, requiring an exact match of the not orthogonal concepts.

We extend the standard vector space method presented by Madylova and Oguducu [9], used by us to create a vector with the introduction of semantic concepts with relations "is-a" and "equivalent-to" not envisaged by the actual method. In the proposed system, an N-dimensional vector represents each report, where N is equal to the number of concepts of the ontology, and 1 indicates the presence of the concept in the report and 0 the absence of such a concept. In this phase, our system is identical to the standard vector space model, that however exploits the knowledge represented in the ontology in terms of relationships "is-a" and "equivalent-to". The vector is populated in agreement with the search of the concepts in the radiological ontology:

- if present, the weight is equal to 1;
- if absent, the weight is 0;

• if there is an “equivalent-to” relationship (“heterogeneous absence"", i.e. "assenza eteroformativa", is the absence of a lesion, and "heteroplastic absence"", i.e. "assenza eteroplasica", is the absence of an alteration of cell growth) the weight will be 1;

• an “is-a” relationship (“fibroadenoma", i.e. "fibroadenoma", that is a benign growth in the breast, is a kind of “benign alterations") takes between all the concepts found in the report the one closest to the root of the ontology, with a weight between 0 and 1 (excluded).

For each concept C that is included between the one closest to the ontology root and the root itself, the weight is calculated using the following equation:

$$Weight(C) = \frac{1}{M} \tag{16}$$

where M is the number of nodes between the root of the ontology. So vectors can have non-orthogonal node C and the concepts proportional to the depth of the possible common ancestor. Once semantic vectors of reports A and B are constructed, the similarity score is expressed using the cosine similarity equation:

$$Similarity = cos(\theta) = \frac{A * B}{\|A\| * \|B\|} = \frac{\sum_{j=1}^{m} A_j \times B_j}{\sqrt{\sum_{j=1}^{m}(A_j)^2 \times \sum_{j=1}^{m}(B_j)^2}} \tag{17}$$

where m is the union of all the concepts in the A and B reports. In Figure 25 a fragment of the used radiological ontology, realized with the

collaboration of experienced radiologists of Policlinic Hospital of Palermo, that describes the implementation of the proposed method is shown.

Figure 25: A fragment of radiological ontology, realized with the collaboration of experienced radiologists of Palermo Policlinico Hospital. "mammo", i.e. "breast", "reperti", i.e. "reports", "X-ray", i.e. "X-ray", "reperti classificati base inte...", i.e. "reports classified based interest", "calcificazioni", i.e. "calcifications", "composizione complessiva mammella", i.e. "overall composition of the breast", "assenza eteroformativa", i.e. "heterogeneous absence", "assenza eteroplasica", i.e. "heteroplastic absence", "fibroadiposo", i.e. "fibrofatty".

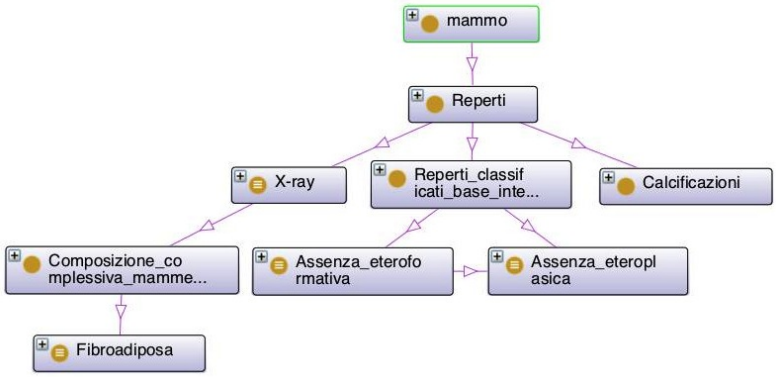

The discussion about experimental results are discussed in Chapter 8.

Chapter 8

Experimental Results

The experimental results for all the previous works are discussed in this section.

8.1 Fingerprint and Iris based Authentication in Inter-cooperative Emerging e-Infrastructures

The measurement indexes used in [1] are the well-known False Acceptance Rate (FAR) and False Rejection Rate (FRR) to detect false positives and false negatives respectively. In order to compare the results with those in the literature and have some scientific value, the protocol used to calculate the number of tests and procedures is that of international competition FVC [43]. Even though the competition was created for fingerprints, from a year or two its criteria became a standard for any type of biometric recognition system. This protocol will be used both for the unimodal and multimodal systems. The protocol provides the following practice tests for the determination of:

- FRR calculation: each sample/image that contains the biometric features of an individual is compared with the remaining samples/images of the same individual. If, during the comparing step the sample g image is compared with the sample h image, then the reverse comparison (i.e., h against g) is not performed to avoid an absolutely obvious and already calculated result;
- FAR calculation: the first sample/image belonging to each individual

is compared with the first sample/image of all individuals, and remaining in the database. If the sample image g corresponds to h, the reverse comparison/symmetric (i.e., h against g) is not performed to avoid an absolutely obvious and already calculated result.

The tests have been performed on two official databases freely downloadable from Internet. As for the system based on fingerprints, will be used the FVC2002 database [53], while as regards the system based on irises will be used the BATH database [54]. From these two databases have been constructed others containing other pairs fingerprint/iris to simulate the acquisition of two biometric features from a generic user. Both used databases are among the most commonly used in science to assess the robustness and performance of recognition systems. The FVC2002 DB2 Fingerprint Database. The FVC2002 DB2 [53] database containing fingerprints was constructed by acquiring images through an optical sensor. This database is divided into two parts, DB2A and DB2B, and is composed of a total of 880 images (800 within the database DB2A and 80 within the database DB2B) belonging to 110 users. For each user 8 images with a resolution of 296x560px have been processed.

The BATH database [44] consists of 2000 images belonging to 50 different ethnic groups of users. For each user are considered left and right eye, capturing 20 images for a total of 40 images for user.

8.1.1 Multimodal Database

To test the proposed fusion technique and the multimodal system various databases were realized. In particular:

- the FVC2002 DB2A-S1 database was generated considering the first 50 members of the original database;
- the FVC2002 DB2A-S2 database was generated by considering the last few 50 users of the original database;
- the BATH-S1 database was generated with 10 users extracted in a very casual way from the original full database. For each user, we have considered the first eight acquisitions of the left eye;
- the BATH-S2 database was generated considering 50 members of the original database. For each user was considered the first eight acquisitions of the left eye;
- the BATH-S3 database was generated considering the same 50 members of the original databases but each of them was considered member of the 8 images acquired at the next 9 to 16.

8.1.2 Fingerprint/Iris Recognition System

Table 4 shows experimental results achieved, in terms of FAR and FRR, in uni-modal and multimodal recognition systems. Table gives the possibility of being able to easily and quickly compare the results obtained with different databases, showing a good level of robustness both in terms of approach used and obtained result:

Table 4: Achieved Experimental Results.

Biometric System	Database	FAR	FRR
Unimodal (Fingerprints)	FVC2002 DB2A-S1	2.86%	17.64%
	FVC2002 DB2A-S2	0.23%	11.77%
Unimodal (Iris)	BATH-S2	1.19%	11.04%
	BATH-S3	1.71%	12.67%
Multimodal	DBtest2	0%	8.19%
	DBtest3	0%	9.7%
	DBtest4	0%	7.28%
	DBtest5	0%	8.16%

For most completeness, the following shows ROC curve relative to tests with database DBtest4. The other curves, obtained with other databases, reported similar characteristics:

Figure 26: ROC curve relative to DBtest4 tests.

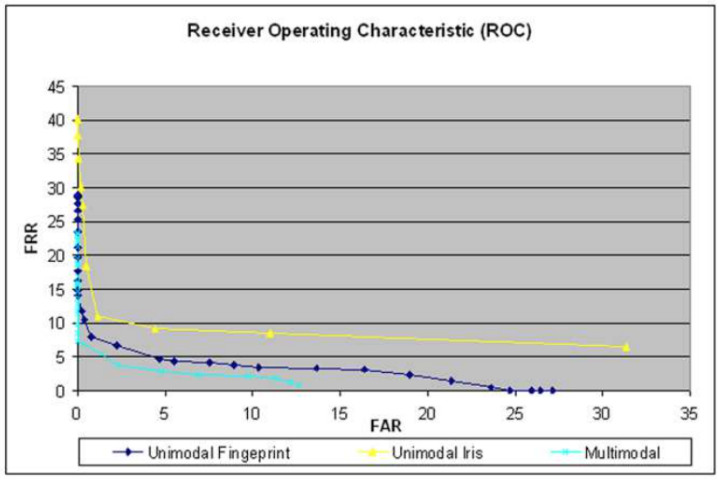

Subsequently, the strategy fusion proposal has been applied and evaluated using data-bases of smaller size. The achieved results are listed the

following Table:

Table 5: Test Databases.

Biometric System	Database	FAR	FRR
Unimodal (Iris)	BATH-S1	0.67%	9.98%
Unimodal (Fingerprint)	FVC2002_DB2B	1.35%	16.78%
Multimodal	DBtest1	0%	5.71%

Figure 27: ROC curve relative to other db tests.

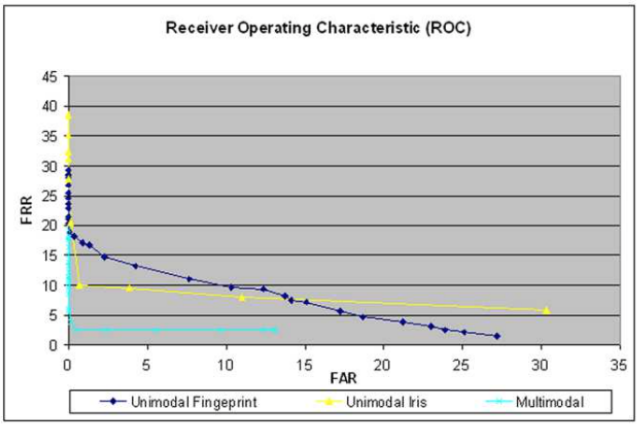

The figure shows that experimental results obtained by multimodal recognition system are maintained below an acceptable threshold, and also comparable to the previous tests, this is sign of a good robustness of system and approach used. This result shows a good performance considering also that for this type of fusion (the template level) there is no weight assigned to the individual results of each multimodal system.

8.1.3 Fingerprint/Fingerprint Recognition System

The Matching Score Level Fusion Module computes the overall matching score combining the two unimodal subsystem matching scores. Since the Micro-CBA Module and the Macro-CBA Module are based on different techniques and parameters to determine the unimodal matching score, a weighted sum, with two different weights, has been used to obtain the overall matching score. Experimental trials have demonstrated that the best performance, in terms of FAR and FRR indexes, is obtained using the following formula: $Global_{Score} = 0.6 * Micro_{score} + 0.4 * Macro_{score}$.

The used FVC2002/DB2B database is composed by gray scale fingerprint images captured by an optical sensor. This database is composed by 80 images of 296x560 pixels, collected from 10 people (8 acquisitions for each people). Table 6 shows the FAR and FRR indexes obtained by the Micro-CBA module and the Macro-CBA module, respectively. In the same table the FAR and FRR indexes of the multimodal system are also listed. FAR and FRR of Micro-CBA Module have been obtained using 12 coincident minutiae for each processed fingerprint pair, as suggested by FBI.

Table 6: Recognition results of the unimodal Micro-CBA module, of the unimodal Macro-CBA module, and of the final multimodal system.

Authentication rates on FVC database	**FAR (%)**	**FRR (%)**
Macro-CBA Module	2.56	18.92
Micro-CBA Module	1.52	20.35
Multimodal System	**1.07**	**10.71**

FAR and FRR of Macro-CBA Module have been computed when the 60% of the directional field of each processed pair is coincident [14]. Multimodal system enhanced accuracy is due to the possibility to correct the wrong results of the first unimodal system using the results achieved by the second unimodal system and viceversa.

8.1.3.1 Hardware FPGA Implementation

Embedded biometric sensors could be a solution to exceed the security limits of the conventional software recognition systems, hiding the most common attack points of a biometric authentication system [56]. An embedded biometric sensor is composed of a biometric scanner for traits acquisition and a hardware processing core. The use of FPGA technology for systems prototyping leads to an acceptable accuracy, great potential speedup, and interesting power consumption feature [57], [58].

The algorithms implementation on FPGA achieves the performance of highly competitive systems. The proposed recognition system takes advantage of FPGA technologies and introduces interesting characteristics considering algorithms used and performance achieved. Table 7 shows the execution times necessary to perform every single authentication task with a working frequency of 25.175 MHz.

Table 7: Execution times of each phase and the relative speed-up factor. The working frequency is 25.175 MHz.

Module	Pre-processing (ms)	Matching (ms)	Total time (ms)	Speed-Up Factor
Micro-CBA	514.1	3.62	517.72	8X
Macro-CBA	34.8		38.42	3X

The speed-up factors are referred to the number of cycles of a general purpose Intel P4@3.00GHz with 2 GB of RAM. The low working frequency suggests interesting considerations for the employment on the embedded recognizer in portable devices, since one of the techniques used to reduce device power consumption is to have a low working frequency with an adequate processing time for the device.

8.1.4 Discussion

In this chapter a multimodal biometric identification system in contrast to the majority of work published on this topic and based on matching-score-level fusion or decision-level fusion has been presented. In fact a template-level fusion method for a multimodal biometric system based on fingerprints and irises has been described. The used approach for fingerprint and iris segmentation, coding, and matching has been tested using the official FVC2002 DB2A fingerprint database and the BATH iris database. Even if, the frequency-based approach, using fingerprint (pseudo) singularity point information, introduces an error on system recognition accuracy, the achieved recognition results have shown an interesting performance if compared with the literature approaches on similar datasets. On the other hand,

in the frequency-based approach, it is very difficult to use the classical minutiae information, due to its great number. In this case, the frequency-based approach should consider a high number of ROIs, resulting in the whole fingerprint image coding, and consequently, in high-dimensional feature vector. In order to test the effectiveness of the described multimodal approach, several datasets have been used. First, two different multimodal systems have been tested and compared on the standard FVC2002 DB2B fingerprint image database and the BATH-S1 iris image database: the former was based on a matching-score-level fusion technique, while the latter was based on the proposed template-level fusion technique.

The obtained results show that the proposed template-level fusion technique carries out an enhanced system showing interesting results in terms of FAR and FRR. The aforementioned result suggests that the template-level fusion gives better performance than the matching-score-level fusion.

Concerning the iris identification system, the achieved performance can be considered very interesting when compared with the results of different approaches found in literature on the same dataset or similar dataset.

The fingerprint/iris multimodal biometric system has been tested on different congruent datasets obtained by the official FVC2002 DB2 fingerprint database and the BATH iris database. The first test conducted on ten users has resulted in FAR = 0% and FRR = 5.71%, while tests conducted on the FVC2002 DB2A and BATH databases resulted in an FAR = 0% and an FRR = 7.28% $\div$ 9.7%. The embedded bio-metric system has been tested on the official FVC2002 DB2B fingerprint database resulting in FAR = 1.07% and FRR = 10.71%.

The described embedded recognizer, using FPGA technology, a smart-card read/write device, and the AES algorithm to cipher the biometric template, shows interesting results in terms of recognition rates.

8.2 A Novel Expert System for Non-Invasive Liver Iron Overload Estimation in Thalassemic Patients

The contributions [35] [36] investigate an ES for classifying liver iron overloading in thalassemic patients. The ES relies on a ANN for mapping a given set of data and for extracting common features and relationships among the data. The mathematical model is trained from an input data set. After the successful training phase, the artificial neural network will be able to perform classification, prediction, or simulation on new data. With more details, the ANN is used for mapping the output of the LIOMOT approach on the output of approach based on MRI T2* assessment for liver iron overload estimation [37].

The former is a SIR (Signal-to-Interference Ratio) based method for estimating the liver iron overloading in medical examinations based only on image processing techniques. The latter is based on relaxation time of T2* method in MRI (Magnetic Resonance Imaging) and it can determine the degree of iron overload on human organs such as liver. LIOMOT output is a continue value between 0 and 1, while the MRI T2* output is a classification of liver iron overload. MRI T2* approach classifies the iron overload in four classes: Normal, Mild, Moderate, and Severe. In this way, each entry of the database is composed of a couple of values, i.e. a value between 0 and 1 given by the LIOMOT method, and one of possible classes produced by the

MRI T2* technique.

The neural network has been trained using the Levenberg-Marquardt back-propagation algorithm, and it maps the continue value produced by the L.I.O.MO.T method with the four classes produced by the MRI T2* method. The dataset is composed of 200 samples. The 75% of the dataset has been used for the training phase, 20% for the validation phase, while the remaining 5% has been used for the test phase. The selected optimal model has been evaluated considering the Mean Square Error (MSE), and the coefficient of correlation (R), and it shows interesting performances. The dataset used for the training-validation-testing phases is composed of patients of Hospital "P. Giaccone" located in Palermo, Italy.

8.2.1 Patients Dataset Description

The proposed method has been tested on real dataset composed of thalassemic patients. The dataset has been collected in the period from October 2010 to August 2011. 131 consecutive patients (64 men and 67 women, mean age 34 $\pm$11 years) affected by thalassemia-major (TM) treated with regular blood transfusion underwent upper abdominal MRI exam to assess liver iron overload between October 2010 and August 2011. MRI was performed using a 1.5-T scanner (GE Excite HDxt, Milwaukee, WI). An eight-element phased-array receiver surface coil was used for signal reception. We used a T2* gradient-echo sequence for liver and pancreas. The scan time for each breath-hold was about 25 seconds (2-3 single end-expiratory breath-holds) and the total scan time was less than 90 seconds. The sequence parameters were as shown in Table 8:

Table 8: Correlation between iron overload detected by Magnetic Resonance Imaging (ms) and Tissue (mg fe/g dry weight)

Matrix	FOV	T.R.	T.E.	Flip Angle	Slice Thickness	Spacing	Bandwidth
256 × 192 pixels	40 × 28 cm	225 ms	3.4 ms	20°	3.0 mm	0	31.2 KHz

8.2.2 Experimental Results

Signal intensity (SI) was measured on a single slice, passing through the portal vein, and it was obtained calculating the mean values of four fixed regions of interest (ROIs) of 0.3 cm^2 placed in the liver and paraspinal muscle in order to obtain the liver-to-muscle SI ratio. Three ROIs were selected in the liver, in order to identify the right lobe, left lobe and periportal space, while the last ROI was placed in the paravertebral muscle (referenced tissue) avoiding artifacts, particularly the decrease of SI adjacent to the posterior lung bases, liver vessels, and heterogeneous areas. Then, we calculated the average of the measurements and the liver-to-muscle SI ratio for each patient. In our statistical evaluation three expert physicians have executed the LIOMOT method. We have estimated the intra and inter-operator variability, as discussed in Section 7.1.3.

The proposed LIOMOT approach has been validated with the use of an Expert System. For each patient, MRI T2* and LIOMOT method have been used for assessment for liver iron overload. The results have been classified through the use of the proposed Expert System, mapping each LIOMOT output with the corresponding MRI T2* class.

The parameters measured for evaluating the performances is the Mean Squared Error (MSE). MSE was computed for training, testing, and validation phases. In addiction, the linear regression of targets relative to outputs has been computed. The proposed ANN was created with the maximum limit of epochs equal to 100, while it converges at epoch 45. In Figure 28 it is possible to see that the MSE for training, testing, validation and global phase is plotted. In particular, the minimum MSE is reached at epoch 39, with value 0.1195.

The four classes of the state-of-the-art method, based on MRI T2* assessment, are shown on x-axes, while L.I.O.MO.T bandwidth values are shown in y-axes. The black line shows the ideal model, while the blue, green, red, and magenta lines indicate the output of the used ANN. The total weighted average in system accuracy was 93%, that is, only 7% of cases were misclassified.

Figure 28: Training, Validation, Test and Overall Mean Square Error. The four classes of the state-of-the-art method, based on MRI T2* assessment, are shown on x-axis, while L.I.O.MO.T bandwidth values are shown in y-axis.

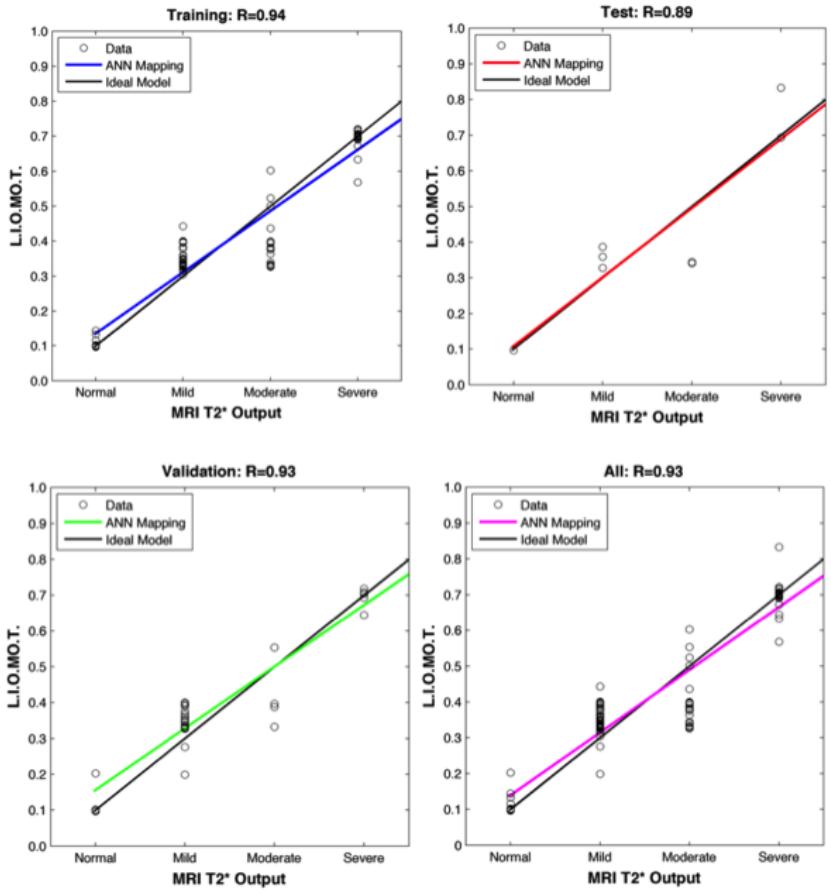

8.2.3 Statistical Analysis

The estimation of the inter-operator variability is calculated with Cronbach alpha coefficient, whereas the Intra-class Correlation Coefficient (ICC) for the intra-operator agreement has been used. The Tables 9 and 10 show the statistical values for Cronbach alpha coefficient and the coefficient for ICC.

The values computed show that the proposed approach has high value of inter and intra-operator variability.

The values computed show that the proposed approach has an high value of Inter and Intra-operator variability. In particular, the high Cronbach's alpha means that the probability of patients misclassification is low, whereas the ICC asserts that the quantitative measurements made by same physician are highly reproducible.

Table 9: Evaluation of inter-operator variability (Cronbach alpha).

	Physician 1 Physician 2	Physician1 Physician 3	Physician 2 Physician 3
Dropping	0.8718	0.8685	0.9593
Total		0.9281	

Table 10: Evaluation of intra variability (Cronbach alpha).

Intra-operator variability (ICC)
0.9101

8.2.4 Discussion

A novel Expert System based on Artificial Neural Network for non-invasive Liver Iron Overload Estimation in Thalassemic Patients has been presented. The ES validates the output of the LIOMOT method through the output obtained from the MRI T2* method. We have achieved this scope using the

proposed Expert System based on Artificial Neural Network. The system validates the LIOMOT method bringing back each case to a specific class of the MRI T2* method, obtaining successful classification in 93% of cases, highlighting the reliability of the proposed algorithm and enabling it as a comparable alternative for investigating liver iron overload with a novel non-invasive method.

8.3 An OsiriX Plugin for Liver Lesion Segmentation

It has been developed a plug-in for a free widespread DICOM viewer software based on a personal computer configured in server function [48], [49]. Images of 50 metastatic patients are been taken from the PACS system using a local high speed network connection, and hepatic findings are been used for scientific purposes. All focal liver lesions were studied both at conventional CT workstation, by an expert radiologist, and by the software automatic evaluation. We analyzed CT images of 50 patients with liver metastases and for each patient was analyzed up to a maximum of three lesions. For each lesion was considered the dimensional and the densitometric criteria and were obtained 3D reconstructions. Results was compared by an other expert radiologist that saw all the images and the software reports.

8.3.1 Patients Dataset

A dataset composed of 50 patients, age between 45 and 75 y., that show liver methastasis have been evaluated. The images have been acquired from a multidetector CT scanner (Brilliance 64, Philips Medical System, Cleveland, Ohio, USA), using the acquisition parameters shown in Table 11:

Table 11: Acquisition Parameters.

Collimation	Gantry Rotation Time	Slice Thickness	Overlap	Reconstruction Image
64 x 0.5 mm	420 ms	1.5 mm	0.7 mm	1 mm

In CT imaging, the lesion's density reflects an intra-tumoral attenuation, expressed in Hounsfield units (Hu). For the RECIST and CHOI criterias, the effectiveness of the evaluation is obtained assessing the affected area, segmenting it from the healthy tissues, and calculating statistical parameters such as mean value, standard deviation and so on.

8.3.2 Experimental Results

A total of 50 patients were evaluated, for an assessment of 190 liver lesions. These lesions were analyzed by two experienced gastrointestinal oncology radiologists, both using an advanced computer station (Agfa HealthCare NV) as well as through the evaluation of the axial images, also of multiplanar reconstructed images (MPR), maximum intensity projection (MIP) and volume rendering (VR), and through the usage of the OsiriX plug-in. Detection and evaluation of dimensional and densitometric changes liver metastases are a time-expensive proceedings in clinical practice. Using an automated software is possible to be better accurate in evaluation of measure and density of focal liver lesions in less time than using the conventional CT workstation.

This tool performs the automatic segmentation of regions of damaged liver, allowing the calculation of values as an average density of the tissues, variance, area, transverse diameter, volume, and reconstruction in 3 dimensions for a better evaluation from the anatomical point of view, and the

generation of a report in spreadsheet format. The strength of a software of this type is the reduction of the intra and inter-operator error, including a significant speedup in the vision and analysis of such images.

8.4 Referenceless Thermometry using Radial Basis Function Interpolation

In this contribution [15] we have compared classical PRF thermometry, Referenceless thermometry, and our novel RBF Referenceless thermometry method. The proposed RBF kernels that we have compared are: Linear RBF, Thin-Plate Spine RBF and Multiquadratic RBF.

8.4.1 Ex-Vivo Thermal Treatment Temperature Assessment

In this trials [15], we have acquired a MRI dataset from a MRgFUS trial treatment on a ex-vivo porcine muscle.

Table 12: MR dataset characteristics used for experimental results.

Dataset Characteristics	Acquisition Protocol	TE/TR	Slice Thickness	Matrix Size
Ex-Vivo animal muscle	Gradient Recall Echo	12.5/25.4	3 mm	256x256

The characteristics of used datasets are showed in Table 12. All the MR images are taken from a GE Sigma HDtx 1.5T scanner, and the ultrasound sonications are performed by an InSightec ExAblate 2100 system. Each sonication takes several seconds to focus high power ultrasounds in the chosen focal point. During each sonication, 9 series of morphological/real/imaginary images are taken, one for each temporal instant. The real and imaginary part are combined together and unwrapped to obtain a phase image.

8.4.2 Experimental Results

The RBF methods have been compared with the polynomial method, using classical PRF shift method as our gold-standard. For each of them has been calculated the Root Mean Square Error (RMSE) between PRF and reconstructed images, and the mean temperature difference against classical PRF. As introduced above, our tests have been conducted performing ultrasound sonication on a ex-vivo porcine muscle (Figure 29). Obtained results are depicted in Tables 13 and 15. In this experiment the RMSE shows that RBF reconstructions has better results with respect to polynomial reconstruction.

Figure 29: Sonication detail in a porcine muscle. The bright part on the left shows the induced protein denaturation.

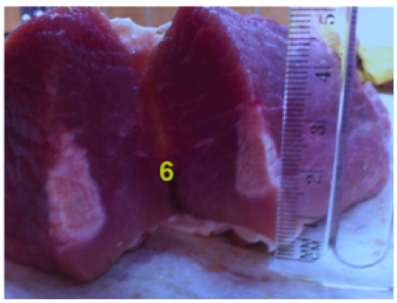

These results are confirmed in Tables 14 and 16, which show the mean values of the temperature reconstructions compared to PRF mean temperature values. In many cases the RBF reconstruction is better than polynomial one. In Figure 29.a, it is possible to see background noise outside to sonicated area (because of PRF shift is affected by relevant noise due to misregistration of phase images). Figure 30 shows the temperature graphs obtained with several reconstructed on sonicated area.

Figure 30: PRF shift classical reconstruction: the typical noise induced by misregistration between different temporal instants is noticeable; b) 5° degree polynomial reconstruction; c) Linear RBF reconstruction; d) Thin-Plate Spline reconstruction.

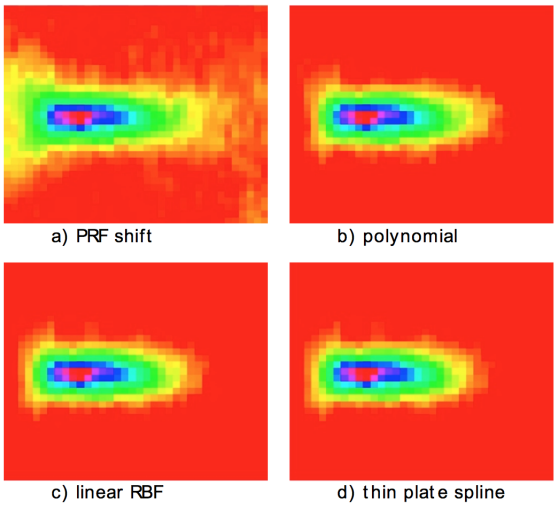

It shows the temperature calculated with standard PRF shift, polynomial method, linear RBF, thin-plate spline RBF, and Multiquadratic RBF for a chosen point along the successive temporal instants of the treatment.

Polynomial reconstruction over-estimates the temperature: this can lead to stop the sonication before reaching the temperature established with the risk of not producing the proteins denaturation as desired.

Figure 31: Temperature rise for each method in the chosen point.

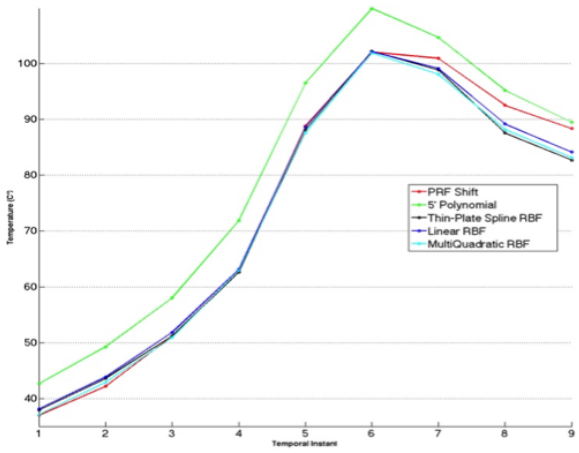

Figure 32 shows the differences between the referenceless methods compared with classical PRF.

Figure 32: Temperature differences obtained from each interpolation method.

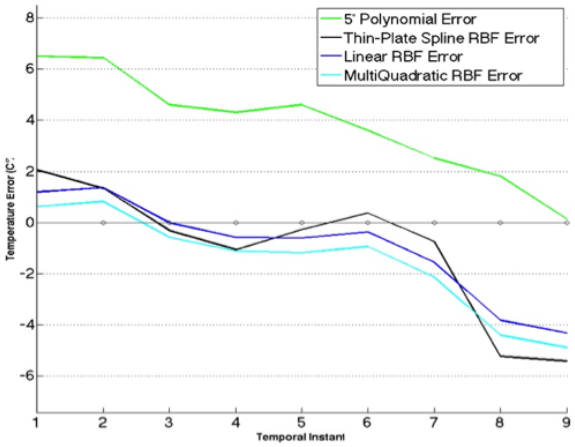

Table 13: MR dataset characteristics used for experimental results.

Temporal Instant	5° Degree Polynomial	Thin-Plate Spline RBF	Linear RBF	Multiquadratic RBF
1	0.034	0.001	0.017	0.022
2	0.041	0.017	0.025	0.036
3	0.070	0.053	0.060	0.065
4	0.086	0.064	0.073	0.062
5	0.066	0.046	0.055	0.043
6	0.065	0.045	0.059	0.066
7	0.075	0.060	0.075	0.058
8	0.119	0.117	0.120	0.123

Table 14: Mean ΔT (°C) With Respect to PRF Approach in #1 Ex-Vivo Sonications.

Temporal Instant	5° Degree Polynomial vs. PRF	Thin-Plate Spline RBF vs. PRF	Linear RBF vs. PRF	Multiquadratic RBF vs. PRF
1	-2.865	-0.121	-1.377	-1.412
2	-3.002	-0.962	-1.661	-1.692
3	-4.208	-2.827	-3.365	-3.397
4	-4.726	-2.890	-3.649	-3.687
5	-4.203	-2.491	-3.230	-3.268
6	-4.114	-2.428	-3.611	-3.647
7	-4.892	-3.653	-4.884	-4.921
8	-5.839	-5.477	-5.732	-5.766

Table 15: R.M.S.E. for #2 Ex-Vivo Experiment

Temporal Instant	5° degree polynomial	thin-plate spline RBF	linear RBF	multiquadratic RBF
1	0.011	0.012	0.011	0.011
2	0.020	0.005	0.002	0.006
3	0.047	0.032	0.034	0.042
4	0.075	0.075	0.070	0.059
5	0.092	0.099	0.086	0.088
6	0.121	0.123	0.117	0.118
7	0.140	0.150	0.140	0.137
8	0.150	0.148	0.145	0.149

Table 16: Mean ΔT (C°) with respect to PRF approach in #2 Ex-Vivo Sonications.

Temporal Instant	5° degree polynomial vs. PRF	thin-plate spline RBF vs. PRF	linear RBF vs. PRF	multiquadratic RBF vs. PRF
1	-0.759	0.840	0.800	0.776
2	-1.190	-0.153	0.072	0.043
3	-1.615	-0.483	-0.643	-0.670
4	-2.246	-2.227	-1.830	-1.852
5	-2.784	-3.282	-2.350	-2.378
6	-3.555	-3.745	-3.311	-3.338
7	-4.201	-4.958	-4.216	-4.245
8	-4.515	-4.329	-4.110	-4.139

As demonstrated, there is an high improvement in Referenceless thermometry using Radial Basis Functions instead of simple Polynomial interpolator.

8.5 RBF Interpolation for Referenceless Thermometry Enhancement

Using the know-how learned and developed in using RBF interpolator for Referenceless thermometry[15], an extension of the method for evaluation

of temperature during real MRgFUS treatments on female patients undergone to uterine fibroma ablation has been proposed [50]. In this contribution classical PRF thermometry, polynomial referenceless thermometry, and the proposed referenceless RBF thermometry have been compared. As aforesaid, Polynomial reconstruction can over/under estimate the temperatures: this can lead to break the sonication before reaching the temperature established. The risk is the missing proteins denaturation, pain inducted in patients, and damage to surrounding tissues. RMS errors and temperature differences show a huge increase of precision in comparison with other kind of interpolators. The obtained results are very promising and suggest that RBF are valid instruments to reconstruct unknown pieces of a surface, estimating coefficients from the data surrounding the sonication area.

8.5.1 In-Vivo MRgFUS Patients Dataset

Ten MR datasets related to ten female patients undergone to MRgFUS treatments for ablation of intra-uterine fibroid have been processed and evaluated. All the MR images are acquired by a GE Signa HDxt 1.5 Tesla scanner, and the ultrasound sonications are performed by an Insightec ExAblate 2100 system. Each hyperthermia sonication takes several seconds to focus high power ultrasounds in the chosen focal point. During each sonication the MR scanner records about 8-12 temporal instants, and each of them is composed of a tern of morphological-real-imaginary images. The real and imaginary parts are combined together to reconstruct phase maps.

8.5.2 Experimental Results

The evaluation of our approach was performed by calculating Root Mean Square (RMS) errors between the original baseline and each reconstructed (Polynomial and our Radial Basis Functions) interpolation, and calculating the differences (in C°) of the mean temperature value between the original PRF temperature and those provided by polynomial and our RBF approach. The kernels here used are the Euclidean, Thin-Plate Spline and the Multi-Quadratic one (Fig. 19).

The natural criterion for assess a reconstructed phase image is how closely it matches the baseline surface prior to the removal of the heated area. The interpolator fitted to the incomplete phase-map is then compared with the original baseline surface. Obtained temperature assessments in a MRgFUS treatment for the ablation of a uterine fibroid are shown in Figure 33.

Figure 33: Temperature reconstruction for a temporal instant during MRgFUS treatment: a) the morphologic MR image; b) temperature assessment using the classical PRF shift method; c) temperature assessment using the Polynomial method; d) temperature assessment using the Linear RBF method; e) temperature assessment using the Multi-Quadratic RBF method; f) temperature assessment using the Thin-Plate Spline RBF method. The depicted values are in °C.

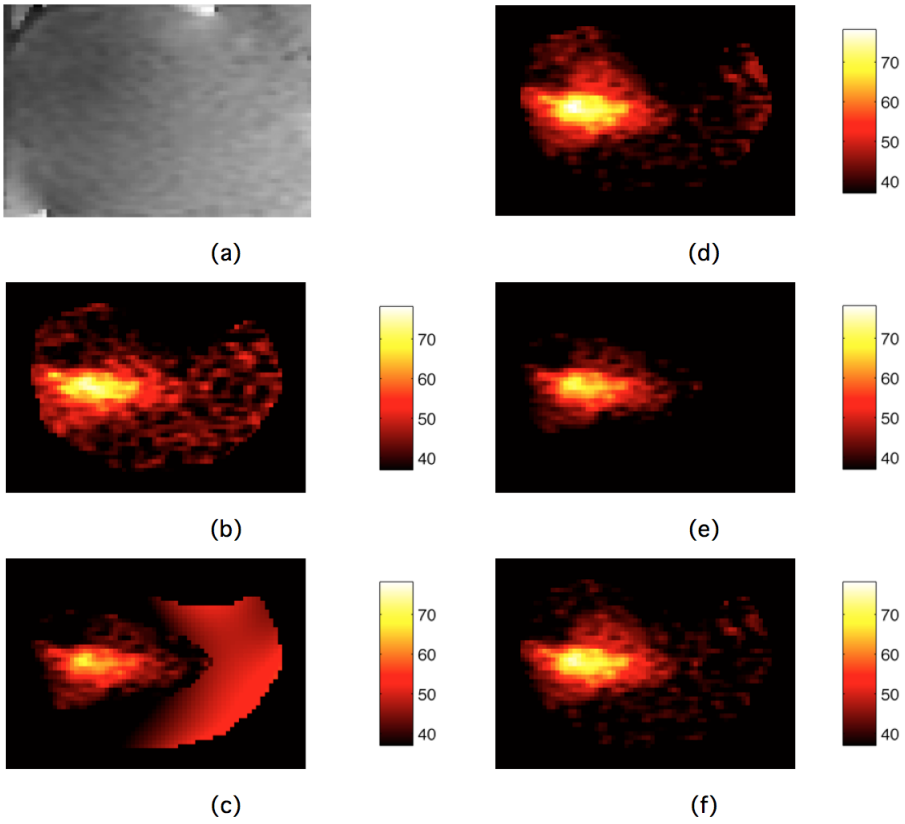

In this figure the RMS error shows that RBF reconstructions (Linear and Multi-Quadratic) has better results with respect to Polynomial reconstruction, assuming that the PRF temperature is the gold standard. Results show a huge increase of precision on the whole reconstructed area.

These results are confirmed in Figure 34, where all the mean tempera-

tures of the treated areas related to thermal treatments of all patients have been compared to PRF temperature.

Figure 34: RMS errors for different kind of reconstruction methods compared to classical PRF Shift thermometry.

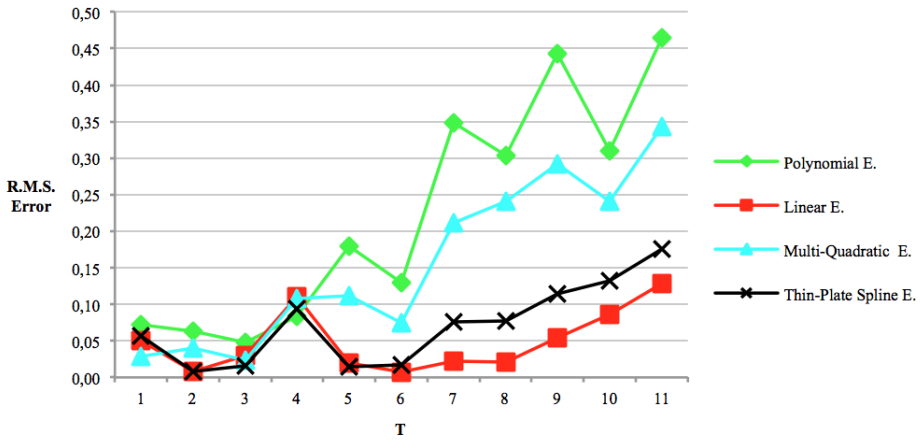

In Figure 34 is depicted to see the temperatures evaluation in a random chosen point of the treatment area. All the RBF-based reconstructed temperatures (the blue, cyan, and black lines) runs very close to the gold standard PRF temperature (red line); we cannot say the same for the polynomial interpolation (green line).

This demonstrates that radial basis functions are a very good kind of interpolator for this type of noisy data, even if there are large regions with missing data.

Figure 35: Mean temperature errors (°C) of the whole area hit by thermal treatment.

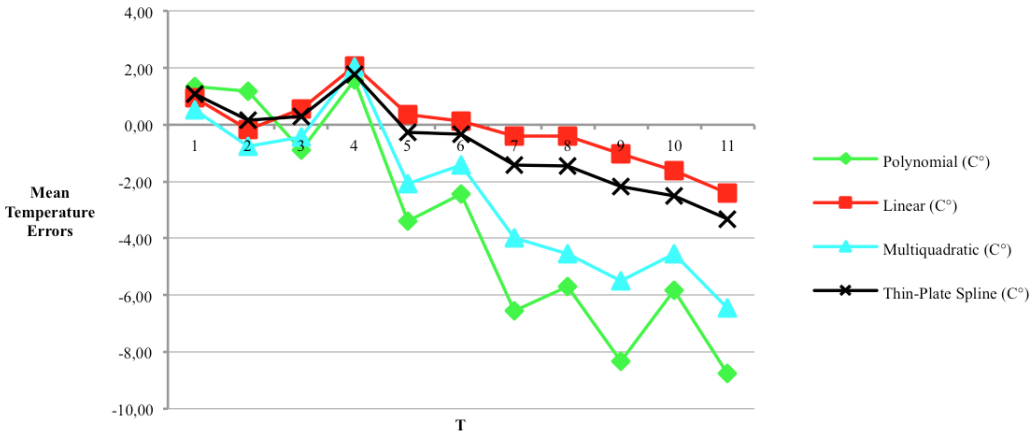

Figure 36: Temperature rise (in °C) for a treatment of about 32 seconds. The red line is the reference PRF temperature, the green line is the Polynomial reconstructed temperature; the black (Thin-Plate Spline), blue (Linear) and cyan (Multi-Quadratic) lines are the RBF-based reconstructed temperatures.

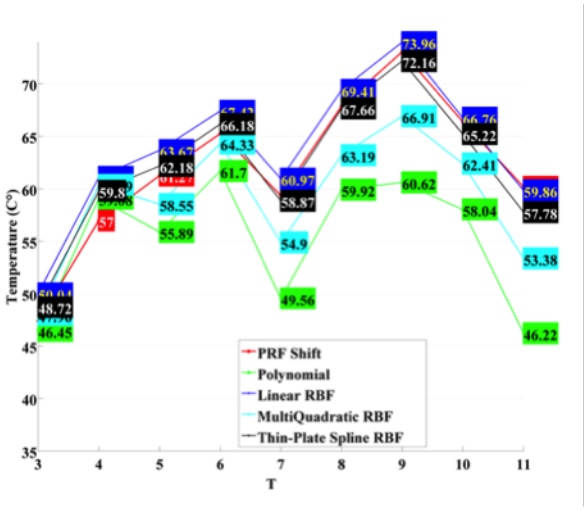

The goodness of the RBF reconstruction is confirmed, for example, in the ninth temporal instant, the PRF temperature is 73.04°C. The RBFs temperatures differs of 3-4°C, while the Polynomial temperature is about 10°C. less. In a MRgFUS treatment, this can lead to continue the sonication process even if it is not necessary, surely causing pain to the patient and possible damages in surrounding tissues.

Figure 37: The variation (error) of reconstructed temperatures compared with the PRF temperature.

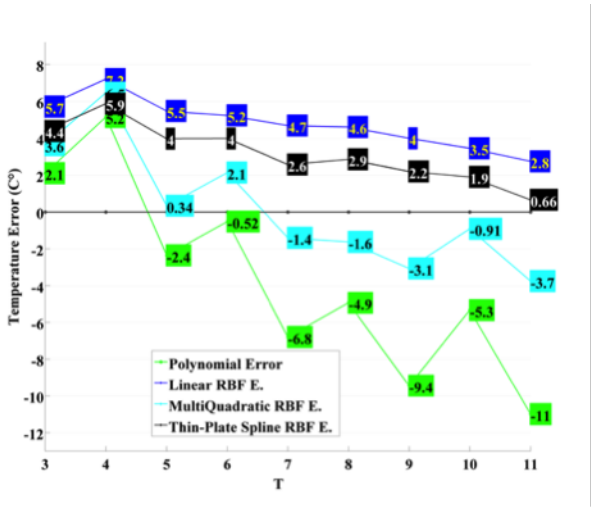

In conclusion, the RBF reconstruction method gains all the advantages of referenceless thermometry avoiding lacks of precision of the Polynomial interpolation temperature reconstruction.

8.5.3 Discussion

In this work classical PRF thermometry, polynomial referenceless thermometry, and the proposed referenceless RBF thermometry have been compared.

The proposed interpolation method has been applied to 2 typologies of datasets: one dataset is relative to an ex-vivo animal muscle, that has been hit by various FUS beams in order to reach high temperatures; the other one is related to several female patients undergone to MRgFUS treatments of uterine fibroma. Polynomial reconstruction can over/under estimate the temperatures: this can lead to break the sonication before reaching the temperature established. The risk is the missing proteins denaturation, pain inducted in patients, and damage to surrounding tissues. RMS errors and temperature differences show a huge increase of precision in comparison with other kind of interpolators. The obtained results are very promising and suggest that RBF are valid instruments to reconstruct unknown pieces of a surface, estimating coefficients from the data surrounding the sonication area.

8.6 Voxel-Based Morphometry

The contribution [55] proposes a novel method that measures the brain' matters (WM, GM, and CSF) in order to assess and quantify their volumetries. The goal of VBM is to assess the presence and the follow-up of matter's reduction, especially in presence of neurodegenerative diseases (i.e. cortical atrophy, dementia, Alzheimer disease). The segmentation and volumetry results has been compared with the results of another widely-used VBM software, FSL. The dataset used for the tests is the IBSR dataset.

8.6.1 IBSR Dataset

The public available IBSR dataset (v2.0), freely downloadable, composed of 18 MR T1 patient acquisitions and the respective manual segmentation has been used in order to evaluate the goodness of the proposed segmentation, not only on the Ground Truth manual segmentation, but also in comparison with the state-of-the-art software used in literature for VBM evaluation. The results are calculated as follows:

- True Positives - TP = voxel considered matter both in reference segmentation and in considered segmentation;
- False Positives - FP = voxel considered to belong to the matter but not considered as such in the segmentation reference;
- False Negatives - FN = voxel excluded from the matter but considered to belong to the matter in the reference;
- True Negatives - VN = voxel excluded both from the reference segmentation, and the calculated segmentation.

The sensitivity, specificity, Dice and Jaccard are calculated as follows:

$$Sensitivity = \frac{TP}{TP + FN} \tag{18}$$

$$Specificity = \frac{TN}{TN + FP} \tag{19}$$

$$Jaccard = \frac{TP}{TP + FN + FP} \tag{20}$$

$$Dice = \frac{2TP}{2TP + FN + FP} \tag{21}$$

Figure 38: In pink, all the voxel correctly labeled from the proposed algorithm; in cyan, all the ground-truth reference voxel. Their intersection are the TP.

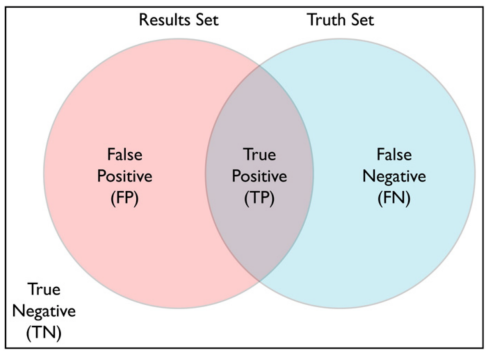

Image resolutions are as depicted in Table 17.

Table 17: Image Resolutions.

# patient	Voxel size (mm3)	X	Y	SLICE
1	1,32	0,9375	0,9375	1,5
2	1,32	0,9375	0,9375	1,5
3	1,32	0,9375	0,9375	1,5
4	1,32	0,9375	0,9375	1,5
5	1,32	0,9375	0,9375	1,5
6	1,32	0,9375	0,9375	1,5
7	1,50	1	1	1,5
8	1,50	1	1	1,5
9	1,50	1	1	1,5
10	1,50	1	1	1,5
11	1,50	1	1	1,5
12	1,50	1	1	1,5
13	1,32	0,9375	0,9375	1,5
14	1,32	0,9375	0,9375	1,5
15	1,05	0,8370	0,8370	1,5
16	1,05	0,8370	0,8370	1,5
17	1,05	0,8370	0,8370	1,5
18	1,05	0,8370	0,8370	1,5

Table 18: The ground-truth volumetry for all the 18 IBSR patient' brains.

#	C.S.F.	Grey Matter	White Matter	Brain
1	78.201	725.132	354.126	1.157.459
2	101.948	675.954	425.432	1.203.334
3	66.265	605.843	287.071	959.179
4	60.644	695.921	323.756	1.080.321
5	109.282	596.162	340.165	1.045.609
6	127.566	575.260	379.514	1.082.340
7	81.379	483.523	305.733	870.635
8	106.942	478.704	287.058	872.704
9	93.645	555.150	358.523	1.007.318
10	120.956	541.347	324.199	986.502
11	82.859	524.859	354.394	962.112
12	113.485	559.844	286.316	959.645
13	68.983	728.698	282.996	1.080.677
14	81.380	694.738	370.382	1.146.500
15	90.750	858.640	433.175	1.382.565
16	92.423	951.201	422.869	1.466.493
17	98.295	1.012.620	464.786	1.575.701
18	113.822	1.051.975	514.842	1.680.639

Each dataset has been segmented by using FSL, SPM, and the proposed system. Sensitivity and specificity indexes, and Jaccard and Dice similarity coefficients have been calculated comparing the output of each software with the ground-truth segmentation provided by the IBSR dataset.

8.6.2 Experimental Results

The proposed segmentation method has been compared with the FSL software, segmenting all the 18 patient's dataset and comparing the obtained results with the ground-truth manual segmentation provided from IBSR dataset. The Table 19 report all the ground-truth volumetry for each matter

that compounds the brain, WM, GM, CSF. The values are expressed in voxels. For the FSL segmentation, the standard segmentation parameters have been used, in order to compare the FSL segmentation with our proposed segmentation. The FSL segmentation results have been compared with the ground-truth segmentation, calculating the sensitivity, specificity, Jaccard, and Dice indexes.

Table 19: The Sensitivity and Specificity indexes of FSL segmentation, compared to Ground-Truth segmentation.

#	Sensitivity CSF	Specificity CSF	Sensitivity GM	Specificity GM	Sensitivity WM	Specificity WM
1	97,69	97,58	60,47	99,65	91,46	99,00
2	96,95	97,93	69,11	99,38	88,67	99,52
3	95,95	98,76	67,93	99,79	94,31	98,94
4	94,88	98,58	65,87	99,78	94,74	98,62
5	96,17	98,39	67,40	99,56	90,09	99,27
6	96,38	98,31	67,77	99,53	90,63	99,44
7	96,58	98,27	66,52	99,38	83,84	99,78
8	93,54	98,49	68,01	99,54	88,39	99,66
9	95,30	98,12	66,18	99,36	86,53	99,63
10	94,50	98,30	69,15	99,41	87,13	99,70
11	93,17	98,12	66,21	99,41	87,51	99,74
12	94,88	98,16	64,62	99,64	91,23	99,47
13	95,06	98,54	63,05	99,81	94,85	98,41
14	97,07	98,60	73,97	99,68	93,18	99,23
15	91,75	97,89	71,54	99,62	94,20	99,13
16	91,76	98,15	70,41	99,73	96,26	98,42
17	91,38	97,68	67,47	99,67	95,13	98,30
18	94,23	97,53	68,88	99,58	94,37	98,54

The depicted values in Table 19 show that there is a poor segmentation for the Grey and White matter, because sensitivity indexes are not so strong. The Jaccard and Dice indexes confirms the segmentation results (Table 20).

In Table 21, we have summarized the segmentation results of the novel method, calculating also in this case the sensitivity and specificity indexes

when compared with the manual segmentation provided by the IBSR ground-truth.

Table 20: The Jaccard and Dice indexes of FSL segmentation, compared to Ground-Truth segmentation.

#	Jaccard CSF	Dice CSF	Jaccard GM	Dice GM	Jaccard WM	Dice WM
1	27,36	42,96	58,30	73,66	74,51	85,39
2	36,18	53,14	64,56	78,47	81,33	89,70
3	37,54	54,59	66,11	79,60	72,62	84,14
4	32,10	48,60	64,30	78,27	70,56	82,74
5	43,28	60,41	63,70	77,82	76,83	86,90
6	45,99	63,01	63,69	77,82	81,00	89,51
7	34,88	51,72	60,37	75,29	79,20	88,39
8	43,07	60,21	63,19	77,44	80,57	89,24
9	35,76	52,68	60,71	75,55	79,91	88,83
10	43,64	60,77	63,72	77,84	81,09	89,56
11	32,29	48,82	60,84	75,66	82,69	90,53
12	40,50	57,65	61,57	76,21	79,25	88,43
13	34,40	51,19	61,80	76,39	65,19	78,93
14	39,95	57,09	71,46	83,36	79,88	88,82
15	31,33	47,71	69,22	81,81	81,25	89,65
16	34,48	51,28	68,97	81,64	74,18	85,18
17	30,94	47,26	65,90	79,44	73,80	84,92
18	33,70	50,41	66,91	80,18	77,13	87,09

We want to highlight that the method is totally automatic and no parameters are provided to the segmentation system. The Table 21 shows the improvement in terms of sensitivity and specificity indexes, showing how the WM recognition, and mainly the GM recognition it has been improved.

The previous results are confirmed in Table 22, where the Jaccard and Dice indexes show the improvement in the correct matter labeling of our method compared to FSL segmentation method.

Table 21: The Sensitivity and Specificity indexes of the proposed segmentation method, compared to Ground-Truth segmentation.

#	Sensitivity CSF	Specificity CSF	Sensitivity GM	Specificity GM	Sensitivity WM	Specificity WM
1	91,74	98,70	80,09	99,05	80,70	99,65
2	87,65	99,18	85,75	98,99	84,39	99,66
3	89,34	99,48	79,43	99,65	92,73	99,09
4	90,59	98,91	78,79	99,53	89,91	99,41
5	86,38	99,51	75,94	99,60	94,73	98,77
6	77,15	99,79	66,05	99,55	97,98	97,81
7	89,14	99,03	69,78	99,77	96,12	99,20
8	87,75	98,97	69,36	99,69	95,19	99,25
9	86,41	99,09	69,78	99,65	95,28	98,90
10	88,18	98,98	67,20	99,72	96,98	98,88
11	88,33	98,88	65,71	99,76	96,40	98,93
12	88,45	98,89	70,08	99,72	96,20	99,11
13	86,21	99,38	82,32	99,48	88,75	99,31
14	91,36	99,44	85,87	99,51	91,43	99,41
15	85,44	98,55	84,23	98,63	78,51	99,82
16	82,94	98,97	80,88	99,09	87,21	98,84
17	79,58	99,10	87,45	98,83	85,11	99,43
18	84,18	99,21	83,92	98,76	85,47	98,81

Table 22: The Jaccard and Dice indexes of the proposed segmentation method, compared to Ground-Truth segmentation.

#	Jaccard CSF	Dice CSF	Jaccard GM	Dice GM	Jaccard WM	Dice WM
1	38,47	55,56	72,80	84,26	74,75	85,55
2	52,62	68,96	76,90	86,94	79,39	88,51
3	53,88	70,03	76,04	86,39	73,71	84,86
4	36,31	53,27	74,90	85,65	78,41	87,90
5	63,01	77,31	72,13	83,81	73,43	84,68
6	67,78	80,80	62,27	76,75	66,99	80,23
7	44,88	61,95	67,22	80,40	79,32	88,47
8	48,88	65,66	66,01	79,52	78,63	88,04
9	47,74	64,62	66,45	79,85	76,39	86,62
10	51,98	68,40	64,58	78,48	75,79	86,23
11	41,54	58,70	63,40	77,60	77,60	87,39
12	48,83	65,62	67,47	80,57	76,82	86,89
13	49,26	66,01	78,08	87,69	74,04	85,09
14	58,24	73,61	81,48	89,80	81,13	89,58
15	36,75	53,75	75,17	85,83	76,04	86,39
16	43,05	60,19	75,51	86,05	71,52	83,39
17	45,17	62,23	80,58	89,25	77,57	87,37
18	53,55	69,75	77,23	87,15	72,35	83,95

Finally, the advantages of our method compared to FSL method are depicted in Table 23 and 24.

Table 23: The Sensitivity and Specificity gain of our method compared to FSL Method.

avg. Sensitivity Gain	avg. Standard Deviation Sensitivity Gain	avg. Specificity Gain	avg. Standard Deviation Specificity Gain
+0,227	-4,254	+0,233	-0,290

Table 24: The Dice and Jaccard gain of our method compared to FSL Method.

avg. Dice Gain	avg. Standard Deviation Dice Gain	avg. Jaccard Gain	avg. Standard Deviation Jaccard Gain
5,550	-4,290	+6,302	-4,196

8.6.3 Discussion

The FSL software is a wide used segmentation software for volumetric brains dataset. It suffers however of almost two defects: (i) the high number of parameters for the system tuning, that increase the segmentation misclassification if the software is used from people that don't know the used algorithms and parameter's choice (e.g. physicist); and (ii) the whole process is rather slow: on modern computers a brain composed of 300-400 slices is segmented at least in 25-30 mins.

Our method employs about 5 minutes for the whole process: 4.30 min for the k-means and training processes, and just 20-30 seconds for the voxel labeling executed by the artificial neural network.

Results are highly comparable and furthermore better than FSL segmentation; the proposed system doesn't require any input parameter. Experimental results shows that the sensitivity and specificity of the system are

absolutely comparable with the FSL results: moreover, many results are superior because closer to the ground-truth values. Dice and Jaccard similarity coefficients confirm the previous results, showing also an improvement in the majority of cases.

8.7 An Ontology-Based Retrieval System for Mammographic Reports

The ontology describes the semantic similarity by means of similarity between concepts contained into unstructured reports . It represents a source of knowledge where medical terms are organized in a hierarchical tree and where it is possible to assess relationships between concepts. The dataset used in this work is composed of 126 unstructured mammographic reports, randomly extracted from the available reports in the Radiological Information System of the University of Palermo Policlinico Hospital. They are written in Italian language.

The developed ontology is composed of 731 concepts, or nodes, having 6 as maximum hierarchy tree depth. The ontology has been developed with the collaboration of three breast imaging expert radiologists. The proposed system computes the report's cosine similarity exploiting semantic vectors and the "is-a" and "equivalent-to" relations [72]. The proposed method shows great improvements if compared against the syntactic classical method

8.7.1 Experimental Results

By locating "fibrofatty", i.e. "fibroadiposo", in the radiological ontology, its depth (shortest distance) in the ontology based on the report "is-a" is shown

in Table 25.

Table 25: Shortest distance for "Fibrofatty" concept node.

Accession Number	Concept Node	Mammo	Finds	X-ray	Finds Classified Based Interest	Fibrofatty
PG286598	Fibroadiposa	4	3	2	1	0

Table 26: Weight for four reports containing (PG286598): "fibrofatty"; (PG287361): "calcifications", "heterogeneous absence", "fibrofatty"; (PG601923): "heteroplastic absence", "fibrofatty"; (PG600585): "heterogeneous absence", "fibrofatty".

Accession Number	Concepts Nodes	Mammo	Finds	X-ray	Finds Classified Based Interest	Calcifications	Overall composition of the breast	Heterogeneous absence	Heteroplastic Absence	Fibrofatty
PG286598	Fibrofatty	1/(1+4)=0,2	1/(1+3)=0,25	1/(1+2)=0,33	-	-	1/(1+1)=0,5	-	-	1/(1+0)=1
PG287361	calcifications	1/(1+2)=0,33	1/(1+1)=0,5	-	-	1/(1+0)=1	-	-	-	-
	heterogeneous absence	1/(1+3)=0,25	1/(1+4)=0,33	-	1/(1+1)=0,5	-	-	1/(1+0)=1	-	-
	Fibrofatty	1/(1+4)=0,2	1/(1+3)=0,25	1/(1+2)=0,33	-	-	1/(1+1)=0,5	-	-	1/(1+0)=1
PG601923	heteroplastic absence	1/(1+3)=0,25	1/(1+2)=0,33	-	1/(1+1)=0,5	-	-	-	1/(1+0)=1	-
	Fibrofatty	1/(1+4)=0,2	1/(1+3)=0,25	1/(1+2)=0,33	-	-	1/(1+1)=0,5	-	-	1/(1+0)=1
PG600585	heterogeneous absence	1/(1+3)=0,25	1/(1+2)=0,33	-	1/(1+1)=0,5	-	-	1/(1+0)=1	-	-
	Fibrofatty	1/(1+4)=0,2	1/(1+3)=0,25	1/(1+2)=0,33	-	-	1/(1+1)=0,5	-	-	1/(1+0)=1

Table 27: Weights in the semantic vectors for three reports compared with the query reports PG601923.

Accession Number	Concepts Nodes	Mammo	Finds	X-ray	Finds Classified Based Interest	Calcifications	Overall composition of the breast	Heterogeneous absence	Heteroplastic Absence	Fibrofatty
PG286598	Fibrofatty	0,2	0,25	0,33	0	0	0,5	0	0	1
PG287361	calcifications heterogeneous absence- Fibrofatty	0,33	0,5	0	0	1	0	1	0	1
PG601923	heteroplastic absence- Fibrofatty	0,25	0,33	0	0,5	0	0	1	1	1
PG600585	heterogeneous absence- Fibrofatty	0,25	0,33	0	0,5	0	0	1	1	1

Table 28: Similarity values for selected reports containing one or more concepts.

Accession Number Reference	Accession Number Comparison	Similarity
PG601923	PG286598	0,60
PG601923	PG287361	0,94
PG601923	PG601923	1
PG601923	PG600585	1

Table 29: The Gold Standard report's classification made by three expert radiologists using twelve categories.

Classes	Concepts Node
1	[Assenza_eteroformativa Fibroadiposa]=[Assenza_eteroplasica Fibroadiposa]
2	[Assenza_eteroformativa Bilaterale Calcificazione_benigna Calcificazioni Fibroadiposa]=[Assenza_eteroplasica Bilaterale Calcificazione_benigna Calcificazioni Fibroadiposa]
3	Assenza_eteroformativa Destra Fibroadiposa
4	Assenza_eteroformativa Consiglia_ecografica Fibroadiposa
5	Assenza_eteroformativa Calcificazione_benigna Calcificazioni Calcificazioni_puntiformi Fibroadiposa Sinistra
6	Assenza_eteroformativa Bilaterale Calcificazione_benigna Calcificazioni Fibroadiposa
7	Assenza_eteroformativa QSE Trasformazione_adiposa
8	[Assenza_eteroformativa Fibroghiandolare]=[Assenza_eteroplasica Fibroghiandolare]
9	[Assenza_eteroformativa Consiglia_ecografica Fibroghiandolare Fibroghiandolare_densa]=[Assenza_eteroplasica Fibroghiandolare Fibroghiandolare_densa Necessaria_integrazione_ecografica]=[Assenza_eteroplasica Consiglia_ecografica Fibroghiandolare Fibroghiandolare_densa]
10	[Assenza_eteroformativa Fibroghiandolare]=[Assenza_eteroplasica Fibroghiandolare]
11	[Assenza_eteroplasica Bilaterale Calcificazione_benigna Calcificazioni Fibroghiandolare]=[Assenza_eteroformativa Bilaterale Calcificazione_benigna Calcificazioni Fibroghiandolare]
12	[Assenza_eteroplasica Fibroghiandolare Fibroghiandolare_densa]

Assigning to the nodes in the ontology a weight calculated by applying the Eq. (16), we obtain the weight of the node "fibrofatty", i.e. "fibroadiposo", as reported in Table 26. When a report has more concepts in the ontology, such as "fibrofatty", i.e. "fibroadiposo", and "heteroplastic absence", i.e. "assenza eteroplasica", the calculation will be done on both nodes, as shown in Table 26, for all the concepts present in the examined reports. Once the weight for each concept of the report present in a node of the ontology is calculated, the semantic vector for the report will be completed, populating it with weights equal to 1 for concepts having relationship "equivalent-to" and with weights between 1 and zero excluded all the ancestors between the concept and the root of the ontology, calculated using Eq. (17) to set the minimum distance between the ancestor and any concept in the document. So vectors can have non-orthogonal concepts proportional to the depth of the possible common ancestor.

Table 27 shows the semantic vectors of the four reports of breast shown in Table 26. The similarity between the vectors of semantic reference to compare (PG601923) and three semantic vectors (PG286598, PG60058 and PG287361) is calculated using Eq. (17). In Table 28 we reported that the similarity values were calculated for some reports containing respectively one, two and three concepts present between the nodes of radiological ontology proving that the calculated similarity value is indicative of the closeness of the semantic content of the two compared reports. In fact, this similarity is equal to 1 by comparing the report PG601923 with himself and with the report PG600585 as submit a report "equivalent-to" between nodes "heteroplastic absence", i.e. "assenza eteroplasica", and "heterogeneous absence",

i.e. "assenza eteroformativa", that makes these two identical concepts. You can see that the similarity between PG601923 and PG287361 is higher but not equal to 1 (0.94 for instance) since they differ only for the "calcifications" concept, that is very close to the root. Finally, the similarity between the PG601923 and PG286598 report is 0.60, because they differ in the concept of "heteroplastic absence", i.e. "assenza eteroplasica", that is much deeper than the root.

The proposed method has been tested on a dataset composed of 126 reports randomly taken from a mammographic report database in the Radiological Information System of the University of Palermo Policlinico Hospital, Italy. They are written in Italian language and they are classified by three expert radiologists in 12 categories (Table 29). To validate the proposed methodology we use semantic vectors to compare reports. The report are classified with values equal to 1 if there is a identical report, according to Eq. (17), obtaining 13 different classes, each of which contains reports identical between them. In order to assess the improvement, the proposed method system has been compared against a standard literature system based on lexical methodology uses Levenshtein distance and k-means clustering with twelve different classes, each of which contains identical reports (such as the classification made by three expert Radiologists in Table 29).

System performances have been evaluated by using several indexes. In Information theory, the reliability of a binary classification test (True/False, Positive/Negative) is generally assessed in terms of Sensitivity (Se) and Specificity (Sp). The two indexes are defined by means of four parameters: True Positive (TP), False Positive (FP), False Negative (FN), and

True Negative (TN):

• True Positive is the number of reports present both in a class of the proposed method and in a class of the classification made by three expert radiologists (gold standard);

• False Positive is the number of reports not present in a class of the proposed method but present in a class of the gold standard;

• False Negative is the number of reports present in a class of the proposed method but not present in a class of the gold standard;

• True Negative is the number of reports not present both in a class of the proposed method and in a class of the gold standard.

Sensitivity measures the percentage of actual positives, which are correctly identified as such, while Specificity measures the percentage of actual negatives. In numerical terms, the two parameters are calculated as follows:

$$Sensitivity = \frac{TP}{TP + FN} \tag{22}$$

$$Specificity = \frac{TN}{TN + FP} \tag{23}$$

To test the reliability of the method proposed, Sensitivity (22) and Specificity (23) have been used, considering two different classification methods.

With the first classification method (Levenshtein distance and k-means clustering), reports with the same distance are selected. Specificity and Sensitivity average values for 12 classes are 53,52% and 100%, respectively (Table 30).

Table 30: True Positive (TP), False Positive (FP), False Negative (FN), and True Negative (TN) of the Proposed Method.

Class	TP	FP	FN	TN
1	41	0	7	78
2	24	0	0	102
3	6	0	42	78
4	2	0	0	124
5	1	0	0	125
6	2	0	0	124
7	3	0	0	123
8	5	0	0	121
9	11	0	0	115
10	8	0	0	118
11	16	0	2	110
12	4	0	0	122
13	2	0	0	124

The second classification method (proposed method), the system selects the reports with similarity equal to "1" with the reference report. The average values of Sensitivity and Specificity for 12 classes are 91,29% and 100%, respectively (Table 31).

Table 31: True Positive (TP), False Positive (FP), False Negative (FN), and True Negative (TN) of the Levenshtein distance and k-means clustering.

Class	TP	FP	FN	TN
1	7	0	41	78
2	17	0	7	102
3	2	0	0	124
4	1	0	0	125
5	1	0	1	124
6	2	0	1	123
7	3	0	2	121
8	4	0	7	115
9	2	0	6	118
10	3	0	13	110
11	2	0	2	122
12	1	0	1	124

The conducted trials show relevant values of Sensitivity if compared against the syntactic classical method, giving rise to the Sensitivity rate of +37,77%. i.e. the developed classifier correctly labels the report in the right gold standard class; moreover, the classifier presents excellent values of

Specificity, i.e. the developed classifier have zero false positives.

8.8 Discussion

In health care domain and in particular in mammography it is important to evaluate the similarity between unstructured clinical reports, allowing the search for similar relevant clinical cases, for instance, to find similar reports for a patient related to the current clinical situation. In this paper a text based indexing system for mammographic similar reports retrieval has been proposed.

The whole system shows interesting results and provides a real-time useful Medical Decision Support System to be used during the referral process. With more detail the method shows great improvements if compared to syntactic classical methods, showing an improvement in Sensitivity of 37,77% and while maintaining a Specificity of 100%. Future directions will aim to integrate heterogeneous clinical data, such as biopsy reports, surgery data, follow-up reports, etc. to build a complete knowledge base addressing the breast pathologies domain. The new data will increase knowledge-based consistency in order to develop innovative Big Data based Medical Decision Support Systems.

This work was partially supported by the Italian “Ministero dell’Istruzione, dell’Università e della Ricerca” under the project PON Smart Cities PON04a2_C “SMART HEALTH - CLUSTEROSDH - SMART FSE - STAYWELL” and under the projects PON PAC "BD4BREAST", project code PAC02L1_00106.

Discussions and Conclusions

In this ph.D. Thesis a series of contributions involving the design, the development, and the implementation of innovative data elaboration techniques coming from heterogeneous imaging sources have been presented.

A part of the activity was focused on medical image segmentation with a significative improvement in some research topics of current interest. At the same time, the developed systems represent improved targets for diagnostic purposes, rising the quality of the work performed by the physician (e.g. reduced errors of measurement, ease/speed of execution of some tasks, etc.).

In biometrics field, two multimodal authentication systems have been investigated, with the combined use of fingerprint and iris biometrical template. The systems are based on matching-score-level fusion or decision-level fusion, and using the official FVC2002 DB2A fingerprint database and the BATH iris database. The obtained results show that the proposed template-level fusion technique carries out an enhanced system showing interesting results in terms of FAR and FRR. The aforementioned result suggests that the template-level fusion gives better performance than the matching-score-level fusion.

For diagnostic purposes, tools for segmentation of medical images from CT liver scans, integrating smart segmentation techniques based on region growing algorithms, has been developed as OsiriX plugin. A dataset composed of 50 patients, for an assessment of 190 liver lesions has been evaluated. The reduction of the intra and inter-operator error, including a significant speedup in the vision and analysis of such images, is the strength of this

contribution.

A novel VBM application for the quantification of cortical atrophies has been proposed. The method clusters and classify the brain' voxels with the use of k-means and neural networks in a totally unsupervised way. The proposed segmentation method has been compared with the FSL VBM software, segmenting all the 18 official IBSR patient's dataset and comparing the obtained results with the ground-truth manual segmentation provided. There is an high improvement of the execution speed of the task, if compared to other VBM software, taking only few minutes to segment a whole T1 MRI brain scan composed from 300 to 400 slices. Results are highly comparable and furthermore better than FSL segmentation; the proposed system doesn't require any input parameter. Experimental results shows that the sensitivity and specificity of the system are absolutely comparable with the FSL results: moreover, many results show high quality since they are closer to the ground-truth values. Dice and Jaccard similarity coefficients confirm the previous results, showing also an improvement in the majority of cases.

It was developed an expert system for data mapping, that investigates the concentration of iron in the liver by imaging methods, and classifies with the use of an ANN. The proposed method has been tested on real dataset composed of 131 consecutive patients affected by thalassemia-major, underwent upper abdominal MRI exams to assess liver iron overload. For each patient, two methods have been used for assessment for liver iron overload. The results have been classified obtaining a system accuracy of 93%, that is, only 7% of cases were misclassified. The proposed system has been also developed as an OsiriX plugin.

An application of Radial Basis Functions neural networks, to achieve a substantial improvement in the problem of measuring body' organs temperature using MRI performed during surgery ablation (MRgFUS), have been developed and tested on two different kind of datasets. RMS errors and temperature differences show a huge increase of precision in comparison with other kind of interpolators. The obtained results are very promising and suggest that RBF are valid instruments to reconstruct temperature, avoiding possible sonication's break before reaching the temperature established, with the risk of missing proteins denaturation, pain inducted in patients, and damages to surrounding tissues.

A text based indexing system for mammographic similar reports retrieval has been proposed. The whole system shows interesting results and provides a real-time useful Medical Decision Support System to be used during the referral process. With more detail, the method shows great improvements if compared against the syntactic classical methods, showing an improvement in Sensitivity of 37,77% while maintaining a Specificity of 100%.

Future directions will aim to investigate smart techniques for the medical imaging problematics, but also for the managing and elaboration of Big Data coming from a wide kind of heterogeneous sources, bringing the computer science field increasingly closer and transversal to the medicine science.

References

1. V. Conti, F. Sorbello, S. Vitabile, L. Agnello: “Fingerprint And Iris Based Authentication In Intercooperative Emerging E-Infrastructures”. Internet Of Things And Inter-Cooperative Computational Technologies For Collective Intelligence, Studies in Computational Intelligence, Vol. 460, 2013, pp 433-462, DOI 10.1007/978-3-642-34952-2_18, Springer.

2. Jain, A.; On-Line Fingerprint Verification. IEEE Transaction on Pattern Analysis and Machine Intelligence, Vol.19, n. 4 (1997) 302-314.

3. Conti, V.; Militello, C.; Sorbello, F.; Vitabile. S.; “A Frequency-based Approach for Features Fusion in Fingerprint and Iris Multimodal Biometric Identification Systems”, IEEE Transactions on Systems, Man, and Cybernetics (SMC) Part C: Applications & Reviews, pp. 384-395. ISSN: 1094-6977, doi:10.1109/TSMCC.2010.2045374

4. UK Biometrics Working Group(BWG): “Biometrics Security Concerns” (2003).

5. Sonka, M., Hlavac, V., and Boyle, R., “Image Processing, Analysis, and Machine Vision”, Brooks/Cole Publi shing Company, 1998.

6. Field, D.J.; Relations between the statistics of natural images and the response profiles of cortical cells, Journal of the Optical Society of America, 1987

7. Masek, L.; “Recognition of human Iris patterns for biometric identification”. Master’s thesis, Univ. Western Australia, Australia.

8. Sanchez-Reillo, R.; Sanchez-Avila, C.; de Martin-Roche, D.; “Iris “ Based Biometric Recognition using Dyadic Wavelet Transform”, IEEE Aerospace and Electronic Systems Magazine, October, 2002, pp. 3-6. 26.

9. Canny, J.; "A Computational Approach to Edge Detection", IEEE Transactions on Pattern Analysis and Machine Intelligence, Vol. 8, pp. 679 - 698 27.

10. Poh Hoon Thian, N.; Bengio, S.; Korczak, J.; “A Multi-Sample Multi-Source Model For Biometric Authentication”, proc. of IDIAP April 2002

11. Patra, P. S. K., Sahu, D. P., & Mandal, I. (2010). An expert system for diagnosis of human diseases. Int. J. Comput. Appl, 1, 13.

12. C.Militello, S.Vitabile, G.Russo, G.Candiano, C.Gagliardo, M.Midiri, M.C. Gilardi, "A semi-automatic multi-seed region- growing approach for uterine

fibroids segmentation in MRgFUS treatment", Proceedings of 7th International Conference on Complex, Intelligent, and Software Intensive Systems, 2013, pp. 176-182

13. Omid, M., Mahmoudi, A., & Omid, M. H. (2010). Development of pistachio sorting system using principal component analysis (PCA) assisted artificial neural network (ANN) of impact acoustics. Expert Systems with Applications, 37(10), 7205-7212

14. Liu, G., Yang, X., Ge, Y., & Miao, Y. (2006). An Artificial Neural Network"based Expert System for Fruit Tree Disease and Insect Pest Diagnosis. In 2006 IEEE International Conference on Networking, Sensing and Control (pp. 1076- 1079).

15. L. Agnello, C. Militello, C. Gagliardo, S. Vitabile: "Referenceless Thermometry using Radial Basis Function Interpolation". Proc. of the International Conference on Computer Medical Applications (ICCMA 2014), World Symposium on Computer Applications & Research (WSCAR 2014), 1-6, DOI 10.1109/WSCAR.2014.6916834.

16. Shah, T. P., & Shah, P. J. (2013). Connectionist Expert System for Medical Diagnosis using ANN"A case study of skin disease Scabies. International Journal, 3(8).

17. Abdul, S., Bhagile, V. D., Manza, R. R., & Ramteke, R. J. Development of an Expert System for Diagnosis and appropriate Medical Prescription of Heart Disease Using SVM and RBF.

18. Gil, D., & Manuel, D. J. (2009). Diagnosing parkinson by using artificial neural networks and support vector machines. Global Journal of Computer Science and Technology, 9(4).

19. J.H.Kim, E.W.Hahn, "Clinical and biological studies of localized hyperthermia", Cancer Res 1979;39:2258"2261.

20. V.Rieke, K.Butts, "MR Thermometry", Journal Of Magnetic Resonance Imaging 27:376"390 (2008).

21. M.Hurwitz, R.Machtinger, F.Fennessy, "Magnetic resonance-guided focused ultrasound surgery for treatment of painful osseous metastases", (2011) Progress in Biomedical Optics and Imaging - Proceedings of SPIE, 7901, art. no. 79010M.

22. C.Militello, S.Vitabile, G.Russo, G.Candiano, C.Gagliardo, M.Midiri, M.C. Gilardi, "A semi-automatic multi-seed region-growing approach for uterine fibroids segmentation in MRgFUS treatment", Proceedings of 7th International Conference on Complex, Intelligent, and Software Intensive Systems, 2013, pp. 176-182

23. K.K.Vigen, B.L. Daniel, J.M.Pauly, K.Butts, "Triggered, navigated, multi-baseline method for proton resonance frequency temperature mapping with respiratory motion", Magn. Reson. Med. 50, 1003" 1010 (2003).

24. A.V.Shmatukha and C.J.G.Bakker, "Correction of proton resonance frequency shift temperature maps for magnetic field disturbances caused by breathing", Phys. Med. Biol. 51, 4689"4705 (2006).

25. S.Roujol, M.Ries, B.Quesson, C.Moonen, and B.D. de Senneville, "Real-time MR-thermometry and dosimetry for interventional guidance on abdominal organs," Magn. Reson. Med. 63, 1080"1087 (2010).

26. V.Rieke, K.K.Vigen, G.Sommer, B.L.Daniel, J.M.Pauly, K.Butts, "Referenceless PRF shift thermometry", Magn Reson Med 2004;51: 1223"1231.

27. K.Kuroda, D.Kokuryo, E.Kumamoto, K.Suzuki, Y .Matsuoka, B.Keserci, "Optimization of self-reference thermometry using complex field estimation", Magn Reson Med 2006;56:835"843.

28. Jain R. et al, Machine Vision, McGraw-Hill, Inc. 1995.

29. Sonka, M., Hlavac, V., and Boyle, R., "Image Processing, Analysis, and Machine Vision", Brooks/Cole Publi shing Company, 1998.

30. Zucker, S. W., "Region growing: Childhood and adolescence", Computer Graphics and Image Processing, 1976, 5, 382-399.

31. Yuan, H., Mao, Z., & Zhao, B. (2010, August). Expert system based on CBR and grey BP for Vannamei disease diagnosis. In Fuzzy Systems and Knowledge Discovery (FSKD), 2010 Seventh International Conference on (Vol. 3, pp. 1015-1019). IEEE.

32. Chavhan GB, Babyn PS, Thomas B, Shroff MM, Haacke EM. Principles, techniques, and applications of T2*-based MR imaging and its special applications. Radiographics 2009;Sep-Oct;29(5):1433-49. doi: 10.1148/rg.295095034.

33. De Almeida Ver_ssimo, M. P., Loggetto, S. R., Junior, A. F., Baldanzi, G. R., Hamerschlak, N., Fernandes, J. L., Galanello, R. (2013). Brazilian Thalassemia Association protocol for iron chelation therapy in patients under regular transfusion. Revista brasileira de hematologia e hemoterapia, 35(6), 428.

34. Rosset, A., Spadola, L., & Ratib, O. (2004). OsiriX: an open- source software for navigating in multidimensional DICOM images. Journal of Digital Imaging, 17(3), 205-216.

35. L. Agnello, A. Farruggia, P. Toia, E. Murmura, M. Russo, E. Grassedonio, M. Midiri, S. Vitabile: "A Novel Expert System for Non-Invasive Liver Iron

Overload Estimation in Thalassemic Patients". The 8th International Conference on Complex, Intelligent, and Software Inten- sive Systems (CISIS-2014), Birmingham, UK, July 2-4, 2014. DOI 10.1109/CISIS.2014.16 3.

36. A. Farruggia, L. Agnello, P. Toia, E. Murmura, M. Russo, E. Grassedonio, M. Midiri, S. Vitabile: "Liver Iron Overload MOnitoring in Thalassemia (LIOMOT) for classifying liver iron concentration in thalassemic patients trough an Artificial Neural Network (ANN)". Sub- mitted to La Radiologia Medica, Springer.

37. Vitabile, S., Gio_, A., Galia, M., La Grutta, L., Lo Re, G., & Midiri, M. (2009). A SIR based method for pancreas iron burden measurement in MRI T2* GRE sequences.. In International Journal of Computer Assisted Radiology and Surgery, Vol. 4, Supp. 1, June 2009 (pp.323-324). Springer.

38. J.H.Kim, E.W.Hahn, "Clinical and biological studies of localized hyperthermia", Cancer Res 1979;39:2258"2261.

39. J. H. Kim, E. W. Hahn, "Clinical and biological studies of localized hyperthermia", Cancer Res 1979;39:2258"2261.

40. M. Hurwitz, R. Machtinger, F. Fennessy, "Magnetic resonance-guided focused ultrasound surgery for treatment of painful osseous metastases", (2011) Progress in Biomedical Optics and Imaging - Proceedings of SPIE, 7901, art. no. 79010M.

41. C. Militello, S. Vitabile, G. Russo, G. Candiano, C. Gagliardo, M. Midiri, M. C. Gilardi, "A semi-automatic multi-seed region-growing approach for uterine fibroids segmentation in MRgFUS treatment", Proceedings of 7th International Conference on Complex, Intelligent, and Software Intensive Systems, 2013, pp. 176-182, DOI: 10.1109/CISIS.2013.36.

42. R.Beatson and G.Newsam, "Fast evaluation of radial basis functions: I", Comput. and Math. with Applicat. 24 (12):7"19, 1992.

43. J.C.Carr, W.R.Fright, R.K.Beatson, "Surface Interpolation with Radial Basis Functions for Medical Imaging", IEEE Transactions On Medical Imaging, Vol. 16, No. 1, February 1997.

44. M.J.D.Powell, "The theory of radial basis function approximation in 1990," in Advances in Numerical Analysis II: Wavelets, Subdivision Algorithms and Radial Functions, W. A. Light, Ed. Oxford, U.K.: Oxford Univ. Press, 1992, pp. 105"210.

45. W.A.Light, "Some aspects of radial basis function approximation," in Approximation Theory, Spline Functions and Applications, S. P. Singh, Ed. Dortrecht, Germany: Kluwer, 1992, pp. 163"190.

46. R.M.Goldstein, H.A.Zebker, C.L.Werner, "Satellite radar interferometry: two-dimensional phase unwrapping", Radio Sci 1988;23:713”720.

47. Alfonso Farruggia, Rosario Magro, Salvatore Vitabile, A text based indexing system for mammographic image retrieval and classification, Future Gener. Comput. Syst. (2014) http://dx.doi.org/10.1016/j.future.2014.02.008.

48. A. Insalaco, L. Agnello, F. Midiri, L. Galbo, M.C. Galfano, M. Galia, et al.: “Creazione di un Plug-In per il Software Open-source di Visualizzazione di Immagini DICOM OsiriX per lo Studio delle Variazioni Dimensionali e Densitometriche di Metastasi Epatiche in TCMS”. Il Giornale Italiano di Radiologia Medica, 1 (Vol. 1), 625-629.

49. D. Picone, L. Agnello, G. Lo Re, M. Galfano, A. Insalaco, F. Muscarneri, et al.: “An Osirix Based Plug-in for the Study of Dimensional and Densitometric Changes of Hepatic Metastases on CT Images”. In Proc. of ECR 2014. Wien : Springer-Verlag Germany, DOI 0.1594/ecr2014/C-0599

50. L. Agnello, C. Militello, C. Gagliardo, S. Vitabile: “Radial Basis Function Interpolation for Referenceless Thermometry Enhancement”. Proc. 16 of Italian Workshop on Neural Networks, Smart Innovation, Systems and Technologies, Springer. To be published.

51. Jenkinson, M., Beckmann, C. F., Behrens, T. E., Woolrich, M. W., & Smith, S. M. (2012). Fsl. Neuroimage, 62(2), 782-790.

52. Friston, K. J. (2003). Statistical parametric mapping. In Neuroscience Databases (pp. 237-250). Springer US.

53. FVC2002, “http://bias.csr.unibo.it/fvc2002/databases.asp”

54. BATH, “http://www.bath.ac.uk/eleceng/research/sipg/irisweb/”

55. L. Agnello, A. Comelli, G. Urso, S. Vitabile, E. Ardizzone: “A Novel Technique for Voxel-Based Morphometry Analysis using K-Means and Neural Networks”. Submitted to the International Journal of Imaging Systems and Technology, John Wiley & Sons Editors.

56. Ambalakat, P.; “Security of Biometric Authentication Systems”, 21st Computer Science Seminar. SA1-T1-1. Page 2

57. Vitabile, S.; Conti, V.; Lentini, G.; Sorbello, F.; “An Intelligent Sensor for Fingerprint Recognition”, Proc. of on International Conference on Embedded and Ubiquitous Compu- ting (EUC-05), Lecture Note in Computer Science (LNCS), Springer-Verlag, vol. 3824, pp. 27-36, ISBN 3-540-30807-5, 2005

58. Militello, C.; Conti, V.; Vitabile, S.; Sorbello, F.; “Embedded Access Points for Trusted Data and Resources Access in HPC Systems”, The Journal of

Supercomputing, - Special Issue on High Performance Trusted Computing, Springer Netherlands, Vol. 55, Number 1, pp: 4-27, ISSN (Print): 0920-8542, ISSN (Online): 1573-0484, DOI: 10.1007s11227-009- 0379-1

59. Jander Moreira and Luciano Da Fontoura Costa, "Neural-based color image segmentation and classification using self-organizing maps", Anais do IX SIBGRAPI, 1996, pp.47-54.

60. Bevilacqua, V., Mastronardi, G., Marinelli M., "A Neural Network Approach to Medical Image Segmentation and Three-Dimensional Reconstruction", DOI 10.1007/11816157_3, Springer Berlin Heidelberg

61. Farruggia, Alfonso, Rosario Magro, and Salvatore Vitabile. "A text based indexing system for mammographic image retrieval and classification." Future Generation Computer Systems 37 (2014): 243- 251.

62. A. Farruggia, R. Magro, S. Vitabile, "Bayesian network based classification of mammography structured report", in: Int. Conference on Computer Medical Applications, (ICCMA 2013), Sousse, Tunisia, 2013, pp. 1–5.

63. A. Farruggia, R. Magro, S. Vitabile, "Novel web service for mammography images indexing", in: The 27th IEEE International Conference on Advanced Information Networking and Applications, (AINA-2013), Barcelona, Spain, 2013, pp. 225–230.

64. J.Mihalcea R, Corley C, Strapparava C. "Corpus-based and knowledge- based measures of text semantic similarity". Proceedings of the 21st national conference on artificial intelligence, vol. 1. Boston, Massachusetts: AAAI Press; 2006. p. 775–80.

65. Pedersen T et al. Measures of semantic similarity and relatedness in the biomedical domain. J Biomed Inform 2007;40(3):288–99.

66. Batet M, Sanchez D, Valls A. An ontology-based measure to compute semantic similarity in biomedicine. J Biomed Inform 2011;44(1):118– 25.

67. Corley C, Mihalcea R. Measuring the semantic similarity of texts. In: Proceedings of the ACL workshop on empirical modeling of semantic equivalence and entailment. Ann Arbor, Michigan: Association for Computational Linguistics; 2005. p. 13–8.

68. Farfan F et al., XOntoRank: ontology-aware search of electronic medical records. In: Proceedings of the 2009 IEEE international conference on data engineering. IEEE Computer Society; 2009. p. 820–31.

69. Pivovarov R, Elhadad N. A hybrid knowledge-based and data-driven approach to identifying semantically similar concepts. J Biomed Inform 2012; 45(3):471–81.

70. Melton GB et al. Inter-patient distance metrics using SNOMED CT defining relationships. J Biomed Inform 2006;39(6):697–705.

71. P. Willett, "The porter stemming algorithm: then and now", Program: Electron. Libr. Inf. Syst. 40 (2006) 219–223.

72. A. Comelli, L. Agnello, S. Vitabile: "An Ontology-Based Retrieval System for Mammographic Reports", submitted to the IEEE Symposium on Computers and Communication, ISCC 2015 (6-9 July 2015), Larnaca, Cyprus.